

A Sino-German $\lambda 6$ cm polarisation survey of the Galactic plane

IX. H II regions

X. Y. Gao^{1,2}, P. Reich³, L. G. Hou^{1,2}, W. Reich³, J. L. Han^{1,2,4}

¹ National Astronomical Observatories, CAS, Jia-20 Datun Road, Chaoyang District, Beijing 100012, PR China

² CAS Key Laboratory of FAST, National Astronomical Observatories, Chinese Academy of Sciences

³ Max-Planck-Institut für Radioastronomie, Auf dem Hügel 69, 53121 Bonn, Germany

⁴ School of Astronomy, University of Chinese Academy of Sciences, Beijing 100049, China

Received; accepted

ABSTRACT

Context. Large-scale radio continuum surveys provide data to get insights into the physical properties of radio sources. H II regions are prominent radio sources produced by thermal emission of ionised gas around young massive stars.

Aims. We identify and analyse H II regions in the Sino-German $\lambda 6$ cm polarisation survey of the Galactic plane.

Methods. Objects with flat radio continuum spectra together with infrared and/or H α emission were identified as H II regions. For H II regions with small apparent sizes, we cross-matched the $\lambda 6$ cm small-diameter source catalogue with the radio H II region catalogue compiled by Paladini and the infrared H II region catalogue based on the WISE data. Effelsberg $\lambda 21$ cm and $\lambda 11$ cm continuum survey data were used to determine source spectra. High angular resolution data from the Canadian Galactic Plane Survey and the NRAO VLA Sky Survey were used to solve the confusion when low angular resolution observations were not sufficient. Extended H II regions were identified by eye by overlaying the Paladini and the WISE H II regions onto the $\lambda 6$ cm survey images for coincidences. The TT-plot method was employed for spectral index verification.

Results. A total of 401 H II regions were identified and their flux densities were determined with the Sino-German $\lambda 6$ cm survey data. In the surveyed area, 76 pairs of sources are found to be duplicated in the Paladini H II region catalogue, mainly due to the non-distinction of previous observations with different angular resolutions, and 78 objects in their catalogue are misclassified as H II regions, being actually planetary nebulae, supernova remnants, or extragalactic sources that have steep spectra. More than 30 H II regions and H II region candidates from our $\lambda 6$ cm survey data, especially extended ones, do not have counterparts in the WISE H II region catalogue, of which 9 are identified for the first time. Our results imply that some more Galactic H II regions still await to be discovered and the combination of multi-domain observations is important for H II region identification. Based on the newly derived radio continuum spectra and the evidence of infrared emission, the previously identified SNRs G11.1–1.0, G20.4+0.1, and G16.4–0.5 are believed to be H II regions.

Key words. ISM: H II regions – Radio continuum: general – Methods: observational

1. Introduction

H II regions are clouds of ionised gas. They appear as flat-spectrum radio sources at higher radio frequencies (usually >1 GHz) when optically thin. H II regions are excellent tracers for Galactic spiral pattern (Hou et al. 2009; Hou & Han 2014). Their emission measures and rotation measures, and hence the derived thermal electron densities and magnetic fields (e.g. Gao et al. 2010; Harvey-Smith et al. 2011) provide important information of the Galactic interstellar medium. The determination of free-free absorption by H II regions at low radio frequencies helps to derive the synchrotron emissivity of our Galaxy (e.g. Su et al. 2017).

Previous large-scale radio continuum and recombination line surveys revealed a large number of H II regions (e.g. Altenhoff et al. 1970; Caswell & Haynes 1987; Kuchar & Clark 1997). By selecting from 24 published lists and catalogues, Paladini et al. (2003) compiled a widely used radio catalogue of Galactic H II regions containing 1442 entries. Recently, through large surveys of radio recombination lines (RRLs) car-

ried out by big dishes such as the Arecibo and Green Bank telescopes, many more new H II regions have been discovered (e.g. Anderson et al. 2011; Bania et al. 2012). A catalogue including over 8 000 Galactic H II regions and H II region candidates from the Wide-field Infrared Survey Explorer (WISE) data was compiled by Anderson et al. (2014). The updated version¹ of this catalogue has been made publicly available after including the follow-up work of Anderson et al. (2015); Makai et al. (2017), and Anderson et al. (2018).

The Sino-German $\lambda 6$ cm polarisation survey of the Galactic plane (Sun et al. 2007; Gao et al. 2010; Sun et al. 2011b; Xiao et al. 2011) surveyed the Galactic disc from $\ell = 10^\circ$ to 230° in Galactic longitude and between $b = \pm 5^\circ$ in Galactic latitude. It provides a large field in which to identify Galactic H II regions. High-frequency radio data are ideal for detecting very young H II regions, which are often optically thick at low frequencies. Moreover, H II regions with a flat spectrum for the thermal bremsstrahlung emission become more pronounced at high radio frequencies than synchrotron radio sources, which have steep spectrum and dominate at lower frequencies (Sun et al. 2011b;

Send offprint requests to: X. Y. Gao and P. Reich
e-mail: xygao@nao.cas.cn, preich@mpi-fr-bonn.mpg.de

¹ <http://astro.phys.wvu.edu/wise/>

Xu et al. 2013a). From this survey, several new H II regions have already been identified, i.e. G124.0+1.4 and G124.9+0.1 in Sun et al. (2007), G148.8+2.3, G149.5+0.0 (possible part of H II region SH 2-205) and G169.9+2.0 in Shi et al. (2008), and G98.3–1.6 and G119.6+0.4 in Xiao et al. (2011). A large $\lambda 6$ cm H II region catalogue was presented by Kuchar & Clark (1997) based on high angular resolution survey images obtained by the telescopes at Green Bank (87GB survey, Condon et al. 1989, hereafter 87GB) and Parkes (Parkes-MIT-NRAO surveys, Condon et al. 1993; Tasker et al. 1994, hereafter PMN). It contains 760 Galactic H II regions with sizes ranging up to $10'$. The Sino-German $\lambda 6$ cm data with a beam size of $9.5'$ can be used for comparison with the small-diameter H II regions in Kuchar & Clark (1997), and also to complement new and larger H II regions with sizes exceeding $10'$.

In this work we identify and analyse H II regions in the Sino-German $\lambda 6$ cm survey. We briefly introduce the data used in Sect. 2. In Sect. 3 we discuss the method for H II region identification. We show the results in Sect. 4, and summarise in Sect. 5.

2. Data

2.1. Urumqi $\lambda 6$ cm data

The Sino-German $\lambda 6$ cm polarisation survey of the Galactic plane² was carried out with the Urumqi 25m radio telescope of the Xinjiang Astronomical Observatory, Chinese Academy of Sciences. The telescope was equipped with a dual-channel $\lambda 6$ cm receiver constructed at the Max-Planck-Institut für Radioastronomie, Germany, which worked at a central observing frequency of 4800 MHz with a bandwidth of 600 MHz, or at 4963 MHz with a reduced bandwidth of 295 MHz to avoid interference. The angular resolution of the survey is $9.5' \times 9.5'$ and the sensitivity is about $1 \text{ mK } T_b$. The total intensity calibration for all observations was based on the calibrators 3C286, 3C48, and 3C138. Descriptions of a detailed system set-up and data reduction can be found in Sun et al. (2006, 2007) and Gao et al. (2010). From the $\lambda 6$ cm survey, Reich et al. (2014) identified 3 832³ small-diameter sources with apparent sizes of less than $16'$ via two-dimensional elliptical Gaussian fits. The fitted major and minor axes were recorded together with the position angles with respect to the north Galactic pole. The positional accuracy is better than $1'$, found by comparing with point sources of the high angular resolution NRAO VLA Sky Survey (NVSS) (Condon et al. 1998). In this work the information (e.g. positions, sizes, and flux densities) of the $\lambda 6$ cm small-diameter sources are taken from Reich et al. (2014).

2.2. Effelsberg $\lambda 11$ cm data

The Effelsberg $\lambda 11$ cm Galactic plane survey was conducted with the Effelsberg 100m radio telescope (Reich et al. 1984, 1990a; Fürst et al. 1990b). The angular resolution of the $\lambda 11$ cm survey is $4.3' \times 4.3'$. The sensitivity is about $20 \text{ mK } T_b$. The survey covers the Galactic plane from $358^\circ \leq \ell \leq 240^\circ$ and $|b| \leq 5^\circ$, and can therefore be used for a full comparison with the Urumqi

$\lambda 6$ cm survey. A catalogue that includes 6 483 $\lambda 11$ cm small-diameter sources with apparent sizes up to $12'$ was compiled by Fürst et al. (1990a). We compiled an additional version of the Effelsberg $\lambda 11$ cm source catalogue after convolving the data to $9.4'$ in order to compare the $\lambda 11$ cm data to the Effelsberg $\lambda 21$ cm data at the same angular resolution. These data were used when the $\lambda 11$ cm data at $4.3'$ resolution did not cover the entire H II region.

2.3. Effelsberg $\lambda 21$ cm data

The Effelsberg 100m radio telescope was also used for a $\lambda 21$ cm Galactic plane survey (Reich et al. 1990b, 1997). The angular resolution of the Effelsberg $\lambda 21$ cm data is $9.4' \times 9.4'$, similar to that of the Urumqi $\lambda 6$ cm survey. The sensitivity of the total intensity data is about $40 \text{ mK } T_b$. The survey covered the range in Galactic longitude nearly identical to the Effelsberg $\lambda 11$ cm survey, being $357^\circ \leq \ell \leq 240^\circ$, but the Galactic latitude range is limited to $|b| \leq 4^\circ$. A total of 2 714 point-like sources have been identified in the survey (Reich et al. 1990b, 1997). Both the Effelsberg $\lambda 11$ cm and $\lambda 21$ cm data play important roles in determining source spectra together with the Urumqi $\lambda 6$ cm data.

2.4. Canadian Galactic Plane Survey $\lambda 21$ cm data

By using the synthesis telescopes of the Dominion Radio Astrophysical Observatory, the Canadian Galactic Plane Survey (CGPS) mapped the Galactic plane at $\lambda 21$ cm within the range of $66^\circ \leq \ell \leq 175^\circ$ and $-3^\circ < b < 5^\circ$ (Taylor et al. 2003; Landecker et al. 2010). The missing large-scale total-intensity emission of the interferometer data was compensated by the data from the Stockert $\lambda 21$ cm survey (Reich 1982; Reich & Reich 1986). The angular resolution of the CGPS data is about $\sim 1'$, ideal for resolving Galactic sources, especially in confused areas where the Urumqi $\lambda 6$ cm beam size is too large.

2.5. NVSS $\lambda 21$ cm data

The NRAO VLA Sky Survey is a $\lambda 21$ cm interferometric continuum survey covering the entire sky of declination $\delta > -40^\circ$ (Condon et al. 1998). The survey provides images with an angular resolution of $45''$ and a catalogue that contains over 1.8 million discrete sources. They were used to extract radio continuum information where CGPS data are absent in this work. As mentioned by Condon et al. (1998), the flux density of extended sources with sizes more than a few times the beamwidth will be missing due to the lack of shorting spacings. Therefore, the NVSS data can only be used for point-like sources and as a hint for structures that are not too extended.

2.6. WISE H II region catalogue

By analysing the WISE mid-infrared images ($\lambda = 3.4, 4.6, 12,$ and $22 \mu\text{m}$ at a resolution of $6''.1, 6''.4, 6''.5,$ and $12''.0$, respectively), Anderson et al. (2014) compiled an infrared H II region and H II region candidate catalogue, covering all Galactic longitudes with Galactic latitude $|b| \leq 8^\circ$. Four types were classified in the catalogue by comparison with the high angular resolution radio interferometric survey data (e.g. CGPS, NVSS). Known H II regions are labelled ‘K’, representing the H II regions that have either radio recombination line measurements or measured H α emission; ‘G’ stands for a group of known H II regions and several H II region candidates where H II region candidates are

² The $\lambda 6$ cm survey data can be downloaded from www.mpifr-bonn.mpg.de/survey.html or <http://zmtt.bao.ac.cn/6cm/surveydata.html>

³ The $\lambda 6$ cm sources at $\ell = 13^\circ 377, b = 0^\circ 136$ and $\ell = 13^\circ 404, b = 0^\circ 147$ are replaced by $\ell = 13^\circ 356, b = 0^\circ 125$ and $\ell = 13^\circ 178, b = 0^\circ 045$ through refit. Two additional $\lambda 6$ cm sources at $\ell = 41^\circ 224, b = 0^\circ 354$ and $\ell = 63^\circ 041, b = -0^\circ 344$ determined by Gaussian fitting are added in this work.

Table 1. Surveys compiled by Paladini et al. (2003) that overlap the $\lambda 6$ cm survey region. The results of the 10 GHz continuum survey from Handa et al. (1987) are incorporated for comparison.

Abbreviation – Reference	telescopes	observing frequency (GHz)	HPBW (')
F72 – Felli & Churchwell (1972)	NRAO 300 feet	1.4, continuum	10
A70 – Altenhoff et al. (1970)	NRAO 300 / 140 feet / Ft. Davis 85 feet	1.4/2.7/5.0, continuum	$9.4 \times 10.4 / 10.9 \times 11.7 / 10.8 \times 10.8$
B69 – Beard & Kerr (1969)	Parkes 64m	1.4/2.7, continuum	14.0 / 7.4
D70 – Day et al. (1970)	Parkes 64m	2.7, continuum	8.2
G70 – Goss & Day (1970)	Parkes 64m	2.7, continuum	8
W70 – Wendker (1970)	NRAO 140 feet	2.7, continuum	10.6×11.6
R86 – Reich et al. (1986)	Effelsberg 100m	2.7, continuum	4.27
F87 – Fürst et al. (1987)	Effelsberg 100m	2.7, continuum	4.27
M67 – Mezger & Henderson (1967)	NRAO 140 feet	5.0, continuum	6.45×6.3
Wil70 – Wilson et al. (1970) [†]	Parkes 64m	5.0, H _{109α}	4
R70 – Reifenstein et al. (1970)	NRAO 140 feet	5.0, H _{109α} and continuum	6.5
A78 – Altenhoff et al. (1978) [*]	Effelsberg 100m	4.9, continuum	2.6
D80 – Downes et al. (1980) ^{††}	Effelsberg 100m	4.9/4.8, H _{110α} and H ₂ CO	2.6
C87 – Caswell & Haynes (1987) ^{†††}	Parkes 64m	5, H _{109α} and H _{110α}	4.4
K97 – Kuchar & Clark (1997)	NRAO 300 feet / Parkes 64m	4.9, continuum	$3.7 \times 3.3 / 5.0^{\dagger\dagger\dagger}$
W82 – Wink et al. (1982)	Effelsberg 100m / Tucson 11m	4.9/14.8/86, continuum	$2.6/1.0/1.3$
H87 – Handa et al. (1987)	Nobeyama 45m	10.05/10.55, continuum	3
W83 – Wink et al. (1983)	Effelsberg 100m	14.7, H _{76α} and continuum	1

Notes. * ADS gave Altenhoff et al. (1979), but it should be Altenhoff et al. (1978).

[†] continuum data mainly from Goss & Shaver (1970).

^{††} continuum results from A78;

^{†††} continuum results from Haynes et al. (1978, 1979);

^{††††} 3.7×3.3 for 87GB and 5.0 for PMN surveys.

located on or within the photo-dissociation region of the known H II region; H II region candidates labelled ‘C’ are objects that have characteristic H II region mid-infrared (MIR) morphology and a radio emission counterpart, but without RRL or H α observations; radio-quiet H II region candidates ‘Q’ meet all the conditions of ‘C’, but without radio counterparts. After adding and removing some sources, there are 8407 total entries of the newest WISE H II region catalogue.

3. Methodology: identification of H II regions

To identify H II regions in the Sino-German $\lambda 6$ cm survey, we separated the Urumqi $\lambda 6$ cm sources into two groups: small-diameter sources from Reich et al. (2014) and extended sources (apparent size $> 16'$) that have not been catalogued yet. In this work, we only consider H II regions whose boundaries and flux densities can be reliably determined by the Urumqi data.

To identify small-diameter H II regions, the intrinsic sizes of Reich et al. (2014) sources were first calculated by deconvolution following

$$\begin{aligned}\theta_{maj} &= \sqrt{\theta_{fit,maj}^2 - 9'.5^2}, \\ \theta_{min} &= \sqrt{\theta_{fit,min}^2 - 9'.5^2},\end{aligned}\quad (1)$$

where θ_{fit} represent the fitted sizes of the major and minor axes of the $\lambda 6$ cm source in Reich et al. (2014) and $9'.5$ is the angular resolution of the Urumqi survey. A cross-match was made between the Urumqi $\lambda 6$ cm small-diameter sources and the Paladini H II region catalogue. To obtain a redundant sample, a loose matching condition was set that the distance for the coincidence must be less than or equal to $r_p + r_{\sigma_p} + r_{6cm} + r_{\sigma_{6cm}} + r_{error}$, where r_p and r_{σ_p} are the source radii and errors given by Paladini et al. (2003), and r_{6cm} , $r_{\sigma_{6cm}}$, and r_{error} are the deconvolved half width of the major axis (θ_{maj}) of the $\lambda 6$ cm sources, their errors, and the positional errors given in Reich et al. (2014). We obtained a total of 419 matching pairs for small-diameter H II regions. The Paladini H II region catalogue includes 1442 entries, of which 777 objects from 17 catalogues are located in the area of the

Urumqi survey (see Table 1). Unfortunately, the positional accuracy given in the Paladini catalogue is limited to 0'.1 in Galactic coordinates. Hence, we had to extract the source positions from the original literature. One Paladini source often has several measurements at various frequencies with different central coordinates. Preference is given to the observation that is more recent, where the observing frequency is closer to 4.8 GHz, and/or where the angular resolution is higher. According to Table 1, the priority sequence follows Kuchar & Clark (1997, hereafter K97), the 4.9 GHz data of Wink et al. (1982, hereafter W82), Altenhoff et al. (1978, hereafter A78), Wilson et al. (1970, hereafter Wil70), Caswell & Haynes (1987, hereafter C87), Reifenstein et al. (1970, hereafter R70), Mezger & Henderson (1967, hereafter M67), Beard & Kerr (1969, hereafter B69), Goss & Day (1970, hereafter G70)/Day et al. (1970, hereafter D70), and Altenhoff et al. (1970, hereafter A70). We also have data from other references; for example, Downes et al. (1980, hereafter D80) observed H_{110 α} and H₂CO for some H II regions. Their continuum parameters were taken from A78 and the flux densities of the sources were re-estimated from the peak flux densities given in A78. Therefore, the flux densities reported by D80 are often nearly identical to those of A78. Similarly, C87 measured H_{109 α} and H_{110 α} , and W70 measured H_{109 α} of some H II regions and their continuum results are taken from Haynes et al. (1978, 1979) and Goss & Shaver (1970), respectively. Although observations above 14 GHz (Wink et al. 1982, 1983, hereafter W82 and W83) have the highest angular resolution, their coordinates are not given priority because they may only show small compact components. Reich et al. (1986) and Fürst et al. (1987, hereafter R86 and F87, which were interchanged in the Paladini H II region catalogue) studied 9 and 11 Galactic objects, respectively, of which 5 and 7 were identified as H II regions. Several surveys (e.g. Felli & Churchwell 1972; Wendker 1970, hereafter F72 and W70) have angular resolutions ($7' \sim 11'$) similar to that of the Urumqi $\lambda 6$ cm survey so that we expected similar observable radio structures and morphologies.

The WISE H II region catalogue introduced in Sect. 2.6 is believed to be the most complete star forming region sample to date. A second cross-match was then made between the Urumqi

$\lambda 6$ cm small-diameter sources and the 4 168 WISE H II region and H II region candidates within the range of the Urumqi survey with the same matching condition as described above.

Anderson et al. (2011) found that the mid-infrared and the radio continuum emission of Galactic H II regions share similar morphologies and angular extents. It was emphasised by Anderson et al. (2014) that the WISE H II regions are related to their radio correspondence based on spatial coincidence. Therefore, we overlaid both the Paladini et al. (2003) objects and the WISE H II regions and H II region candidates whose diameters are larger than $8'$ onto our $\lambda 6$ cm images. Coincidences for extended H II regions were then searched by eye. We also kept those extended sources in the $\lambda 6$ cm image that have not been identified that way. They may be new H II regions. To eliminate the projection effect in the radio-infrared association and to verify the nature of those un-identified extended sources, spectra were fitted using the Effelsberg $\lambda 21$ cm, $\lambda 11$ cm, and the Urumqi $\lambda 6$ cm data, and/or were tested by the TT-plot method (Turtle et al. 1962) for both the small-diameter and the extended sources chosen by the above procedure. The sources that show an optically thin, flat ($\alpha \sim -0.1$, $S_\nu \sim \nu^\alpha$), or a slightly positive spectral index were identified as H II regions. Additional supporting evidence came from H α data (Finkbeiner 2003), the Digitised Sky Survey (Lasker et al. 1990, DSS), and IRIS $60\mu\text{m}$ data (Miville-Deschênes & Lagache 2005). To avoid the inclusion of supernova remnants (SNRs) and planetary nebulae (PNe), the Green SNR catalogue (Green 2017), the Galactic PNe catalogues from Condon & Kaplan (1998), Parker et al. (2006), Miszalski et al. (2008), Frew et al. (2013), Parker et al. (2016), Fragkou et al. (2018), and Irabor et al. (2018) were consulted.

4. Results

After scrutinising the small-diameter and the extended H II regions on the $\lambda 6$ cm images, we identified 401 H II regions in total from the Sino-German $\lambda 6$ cm polarisation survey of the Galactic plane. We list the results in Table 2, Table 3, and Table 4. Full tables can be accessed via CDS. Table 2 contains the $\lambda 6$ cm small-diameter H II regions with counterparts in the Paladini et al. (2003) H II region catalogue. Table 3 includes the $\lambda 6$ cm small-diameter H II regions that have WISE H II region counterparts but were not included in Paladini et al. (2003). Table 4 lists the extended H II regions identified in the Urumqi $\lambda 6$ cm survey. In all these three tables, we provide the central positions of the H II regions, the integrated flux densities especially the new $\lambda 6$ cm results based on the Urumqi data, and distance information from new measurements in the literature if available.

For objects in Table 2, the flux densities based on the Effelsberg $\lambda 21$ cm and $\lambda 11$ cm data were added for comparison. Some of the $\lambda 21$ cm results were re-calculated due to the imperfect determination of the zero levels by the automatic Gaussian fit. Some of the $\lambda 11$ cm results were obtained from the 9/4 resolution data (see Sect. 2) instead of the 4/3 original data, because sometimes the original $\lambda 11$ cm data have only fitted a part of the H II region or the underlying emission influenced the zero levels during fitting. We also list the flux density measurements quoted in the Paladini H II region catalogue for each source in Table 2. However, some errors were noticed: (1) inappropriate flux density assignment, e.g. G24.7–0.2a and G24.7–0.2b, which should have two sets of different values (see K97) but were given the same in the Paladini catalogue; (2) missing flux density, e.g. G45.5+0.1, for which two components of A78 (D80), W82, W83 should be included, but only one was listed; (3) inappropriate estimates of flux density, especially for all the 86 GHz measure-

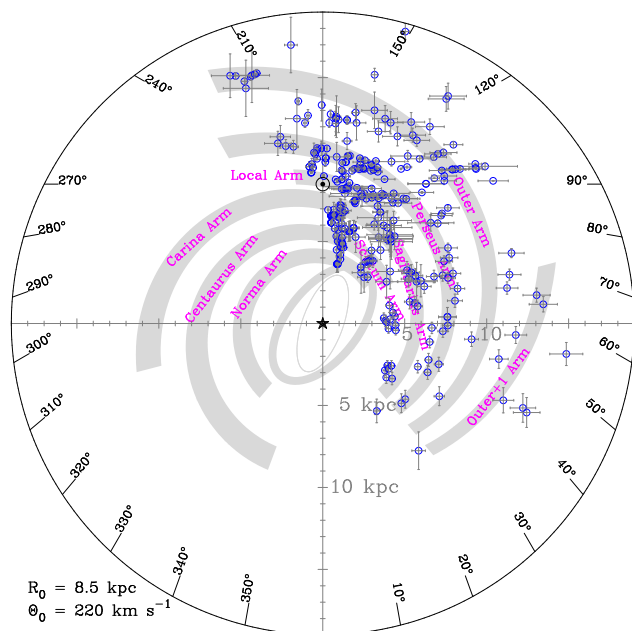


Fig. 1. Distribution on the Galactic plane of H II regions identified in the Urumqi $\lambda 6$ cm survey with known distances.

ments of W82. All these problems were reviewed by checking the original references and fixed. There are still some previous flux density results that cannot be understood easily, such as those from W70. We convolved the 4/3 angular resolution Effelsberg $\lambda 11$ cm data to $11'$, the same as W70 for the Cygnus X region. We took eight isolated sources which are not confused by the strong background emission and estimated their 2.7 GHz flux densities and sizes by Gaussian fit. For most of the cases, the newly derived results from the Effelsberg data are much smaller than those reported by W70.

In Table 3, it is usually the case that one $\lambda 6$ cm radio source is found to have several counterparts in the WISE H II regions. However, due to the limit of the angular resolution of the Urumqi data, we cannot give the exact correspondence, and therefore list all the WISE H II regions included in one $\lambda 6$ cm source. Based on the type classification of the WISE H II regions (see Sect. 2.6), we understand that the Q-type WISE H II regions are the ones that do not yet have radio continuum detection. Thus, Q-type WISE H II regions are not listed if there are also K-, G-, or C-type WISE H II regions for the same $\lambda 6$ cm source.

For the H II regions in Table 4, diffuse Galactic background emission was filtered out by the technique of ‘unsharp-masking’ (Sofue & Reich 1979) prior to the flux density integration. The shape of extended H II regions, unlike the small-diameter sources, often cannot be simply described as circular or elliptical Gaussians. Therefore, the apparent sizes listed in Table 4 were all measured in the directions of Galactic longitude and Galactic latitude. We listed the $\lambda 6$ cm extended H II regions that have WISE H II region counterparts (K-, G-, or C-type) in the upper part of Table 4 (Rows 1 – 74). In the lower part (Rows 75 – 107), we show the $\lambda 6$ cm extended H II regions and H II region candidates which do not have matching WISE H II regions.

We illustrate the distribution of the identified $\lambda 6$ cm H II regions with determined distances onto a bird’s eye view of the Galactic disc in Fig. 1. These H II regions can be traced from the Norma Arm in the Galactic centre to the Outer+1 Arm. Most H II regions are located in the spiral arms, while some are located in the inter-arm area.

Table 2. Small-diameter H II regions identified in the Urumqi $\lambda 6$ cm survey by comparison with the Paladini H II region catalogue.

P number	G-NAME	GLong ($^{\circ}$)	GLat ($^{\circ}$)	Ref	D (kpc)	Ref	EB $S_{21\text{cm}}$ (Jy)	EB $S_{11\text{cm}}$ (Jy)	Urumqi $S_{6\text{cm}}$ (Jy)	S_{Ref} (Jy)	Freq (GHz)	Ref	Notes
129	G10.1–0.4	10.073	–0.412	A78	4.95 \pm 0.51	srn+14	47.01	54.819	63.835	3.00	4.9	A78	included in the $\lambda 6$ cm source G10.16–0.35
131	G10.2–0.4	10.190	–0.426	D80	4.95 \pm 0.51	srn+14	47.01	54.819	63.835	5.1	4.9	D80	included in the $\lambda 6$ cm source G10.16–0.35
132	G10.2–0.3	10.159	–0.349	K97	4.95 \pm 0.51	srn+14	47.01	54.819	63.835	55	2.7	A70	included in the $\lambda 6$ cm source G10.16–0.35
										65	2.7	G70	new 14.7 GHz flux density
										66.353	4.9	K97	
										47	5.0	A70	
										47.48	4.9	A78	
										47.5	4.9	D80	
										63.2	5.0	M67	
										51.8	5.0	R70	
										48.4	5.0	Wil70	
										31.67	10.0	H87	
										<36.6	14.7	W83	
134	G10.3–0.2	10.315	–0.150	K97	4.95 \pm 0.51	srn+14	14.61	13.77	15.923	22	2.7	G70	same as P135
										20.472	4.9	K97	
										12.48	4.9	A78	
										12.5	4.9	D80	
										20.2	5.0	M67	
										<9.2	14.7	W83	
135	G10.3–0.1	10.307	–0.145	R70			14.61	13.77	15.923	20	2.7	A70	same as P134
										20	5.0	A70	
										13.6	5.0	R70	
										10.81	10.0	H87	

Notes. Column 1: sequential number in Paladini et al. (2003); Column 2: G-name of the H II region; Columns 3, 4, and 5: Galactic longitude, latitude, and their reference; Columns 6 and 7: distance for the H II region and reference; Columns 8, 9, and 10: integrated flux densities based on the Effelsberg $\lambda 21$ cm, $\lambda 11$ cm, and the Urumqi $\lambda 6$ cm data. Some of the $\lambda 11$ cm results (with 2 digits) are from the data at original resolution and some (with 3 digits) are from the data which were convolved to an angular resolution of $9''.4$; Columns 11, 12, and 13: integrated flux densities, the corresponding frequencies, and their references. Most of these are based on Paladini et al. (2003), except those of Handa et al. (1987). The flux densities from Paladini et al. (2003) were all examined by comparing the results to the original references. Corrections were made if improper values were found; Column 14: remarks for the source. Full table is accessible from the CDS.

References. brn+09: Brunthaler et al. (2009); chr+14: Choi et al. (2014); fb84: Fich & Blitz (1984); fb15: Foster & Brunt (2015); hbc+07: Honma et al. (2007); hh14: Hou & Han (2014); irm+13: Immer et al. (2013); mdf+11: Moisés et al. (2011); mrm+09: Moscadelli et al. (2009); okh+10: Oh et al. (2010); rus03: Russeil (2003); rag07: Russeil et al. (2007); rbr+10: Rygl et al. (2010); rbs+12: Rygl et al. (2012); srn+14: Sanna et al. (2014); wsr+14: Wu et al. (2014); xrm06: Xu et al. (2006); xlr+13: Xu et al. (2013b); zsr+09: Zhang et al. (2009); zrm+13: Zhang et al. (2013); zms+14: Zhang et al. (2014).

Table 3. $\lambda 6$ cm small-diameter H II regions that have WISE H II region counterparts but are not in the Paladini catalogue.

No.	G-NAME	GLong $_{6\text{cm}}$ ($^{\circ}$)	GLat $_{6\text{cm}}$ ($^{\circ}$)	θ_{maj} ($''$)	θ_{min} ($''$)	$S_{6\text{cm}}$ (Jy)	GLong $_{\text{wise}}$ ($^{\circ}$)	GLat $_{\text{wise}}$ ($^{\circ}$)	diameter ($''$)	WISE type	D (kpc)	Ref	Notes
1	G12.2–0.1	12.232	–0.110	8.4	5.7	5.405	12.145	0.000	13.4	K			one $\lambda 6$ cm source matches thirteen WISE H II regions
							12.184	–0.113	0.7	K			
							12.192	–0.104	1.0	K			
							12.194	–0.144	0.6	K			
							12.194	–0.112	0.6	K			
							12.194	–0.129	1.6	K			
							12.199	–0.034	1.4	K			
							12.202	–0.110	0.8	K			
							12.209	–0.105	0.7	K			
							12.216	–0.119	0.8	K			
							12.217	–0.138	2.3	K			
							12.229	–0.115	2.0	K			
							12.311	–0.059	6.0	K			
2	G19.8+0.3	19.775	0.285	<3.1	<3.1	0.655	19.741	0.280	1.4	K	14.20 \pm 0.61	hh14	one $\lambda 6$ cm source matches two WISE H II regions
							19.781	0.287	3.7	K	17.28 \pm 1.22	hh14	
3	G23.5+1.6	23.547	1.589	<3.1	<3.1	0.147	23.569	1.582	3.9	K	2.94 \pm 0.42	hh14	
4	G26.4+1.5	26.373	1.451	8.1	5.7	1.216	26.385	1.399	19.8	K			one $\lambda 6$ cm source matches two WISE H II regions
							26.385	1.401	3.8	K	3.03 \pm 0.40	hh14	

Notes. Columns 1 and 2: sequential number and G-name; Columns 3 and 4: Galactic longitude and latitude of the $\lambda 6$ cm source; Columns 5 and 6: intrinsic size θ_{maj} and θ_{min} of the $\lambda 6$ cm source, obtained following Eq. (1) by assuming the sources to be Gaussian. The observed sizes ($\theta_{\text{fit,maj}}$ and $\theta_{\text{fit,min}}$) used for the deconvolution are taken from Reich et al. (2014). The Galactic position angle for each source can be found in Reich et al. (2014); Column 7: integrated flux density at $\lambda 6$ cm; Columns 8 and 9: Galactic longitude and latitude of the matched WISE H II region; Column 10: diameter of the matching WISE H II region; Column 11: group type of the WISE H II region, K* indicates currently known H II regions (original C-type WISE H II regions) according to Kim et al. (2018); Columns 12 and 13: distance information and their references; Column 14: remarks for the source. Some other references in the 14th column: e.g. Suad et al. (2012). Full table is accessible from the CDS.

References. abb+14: Anderson et al. (2014); aaj+15: Anderson et al. (2015); aal+18: Anderson et al. (2018); cpt06: Comerón et al. (2006); fb15: Foster & Brunt (2015); hh14: Hou & Han (2014); mdf+11: Moisés et al. (2011); rus03: Russeil (2003); rag07: Russeil et al. (2007); xlr+13: Xu et al. (2013b).

As listed in Table 2 and for some sources in Table 4, Paladini et al. (2003) collected many H II regions which were previously measured at $\lambda 6$ cm. We made a comparison between the new results derived from the Urumqi data and those flux densities quoted in Paladini et al. (2003). We show the result in Fig. 2. The ratio is approximately 1 in general, proving the

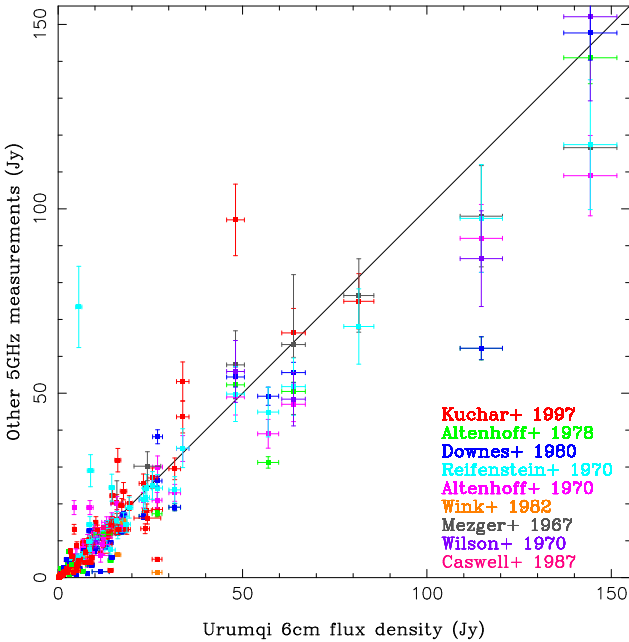
consistency, but the Urumqi flux densities are somewhat higher for those sources with higher flux densities. For some of the sources, one H II region seen in the Urumqi data can be resolved into several components, for example in Altenhoff et al. (1978) and Kuchar & Clark (1997). These components have to be added first, before the comparison. The angular resolu-

Table 4. Extended H II regions in the $\lambda 6$ cm survey.

No.	G-NAME	GLong _{6cm} (°)	GLat _{6cm} (°)	Apparent θ_{maj} (')	Apparent θ_{min} (')	S_{6cm} (Jy)	GLong _{wise} (°)	GLat _{wise} (°)	Diameter (')	D (kpc)	Ref.	Notes
1	G11.7–1.7	11.69	–1.74	19.8	15.7	5.084	11.662	–1.692	30.2	1.6±0.2	rus03	SH 2-37, P150
2	G13.8–0.8	13.80	–0.81	18.0	11.5	12.183	13.776	–0.795	18.1			RCW 156, P176
3	G15.1+3.3	15.11	3.35	22.0	20.3	7.743	15.128	3.310	37.8	2.8±0.6	rus03	SH 2-46, P202
4	G16.9–1.1	16.87	–1.05	21.8	13.9	7.447	16.857	–1.155	23.9			SH 2-50, including P216, see Sun et al. (2011a)
5	G16.9+0.8	16.94	0.77	60	55	162.677	16.993	0.874	37.5	2.0±0.25	rus03	SH 2-49, RCW 165, P218, P219, P220, P224
...												
75	G17.0+1.7	17.02	1.72	27.8	15.7	6.353						P221/P222, flat radio spectrum
76	G20.3–0.9	20.27	–0.89	18.5	13.0	3.560						P266/P267/P268, flat radio spectrum
77	G63.7–0.7	63.65	–0.72	17.0	13.6	0.858						P622, flat radio spectrum
78	G66.4–1.2	66.41	–1.17	100	96	7.874	66.660	–1.167	62.5			DU 34, including P631, Q-type WISE H II region?
79	G68.4+0.2	68.39	0.19	23.6	17.3	1.404						flat radio spectrum, possible infrared emission associated
...												

Notes. Columns 1 and 2: sequential number and G-name; Columns 3 and 4: Galactic longitude and latitude of the $\lambda 6$ cm source; Columns 5 and 6: apparent size θ_{maj} and θ_{min} of the $\lambda 6$ cm source measured in Galactic longitude and latitude directions; Column 7: integrated flux density at $\lambda 6$ cm; Columns 8 and 9: Galactic longitude and latitude of the matched WISE H II region; Column 10: diameter of the matching WISE H II region; Column 11 and 12: distance information and their references; Column 13: remarks for the source. Some other references in the 13th column: e.g. Sieber & Seiradakis (1984), Suad et al. (2012), Gao et al. (2011), Gao & Han (2013), and Graham et al. (1982). Full table is accessible from the CDS.

References. abb+14: Anderson et al. (2014); aaj+15: Anderson et al. (2015); aal+18: Anderson et al. (2018); rmb+09: Reid et al. (2009); chr+14: Choi et al. (2014); fb84: Fich & Blitz (1984); fb15: Foster & Brunt (2015); hh14: Hou & Han (2014); rus03: Russeil (2003); rag07: Russeil et al. (2007).

**Fig. 2.** Flux density comparison between the new $\lambda 6$ cm measurements and previous $\lambda 6$ cm results.

tion of the Urumqi survey is only slightly better than that of Altenhoff et al. (1970), but coarser than all the other eight surveys. Individual components of H II regions or underlying emission were possibly included in $\lambda 6$ cm sources when the Urumqi data cannot resolve them (e.g. $\lambda 6$ cm source G192.6–0.0 includes five H II regions: SH 2-254 to 258). The seeming overestimate of the Urumqi $\lambda 6$ cm results is also caused by the fact that high angular resolution observations did not cover the entire, but only a part of the H II regions, for example G119.4–0.8 from Kuchar & Clark (1997).

There are some interesting newly identified objects in Table 4, and so in the following we first discuss a smaller number of objects in the WISE H II region catalogue, and then talk about many objects in the Paladini H II region catalogue.

4.1. Notes on some objects in the WISE H II region catalogue

WISE H II regions with sizes exceeding $8'$ were used to search for a sample of $\lambda 6$ cm extended H II regions. After excluding the small-diameter H II regions, 107 extended H II regions and H II region candidates whose flux densities can be reliably measured with the Urumqi $\lambda 6$ cm data were catalogued and given in Table 4. Among these sources, more than 30 were found without counterparts in the WISE H II region catalogue. We show an example in Fig. 3. In the WISE $12\mu\text{m}$ infrared image, 12 WISE H II regions (marked with white squares and blue dashed circles) are located in a $3^\circ \times 3^\circ$ area centred at $\ell = 127^\circ 046, b = 0^\circ 950$. Except for G125.606+2.099 (C-type) in the upper right corner, all the other WISE H II regions are Q-type WISE H II regions. They do not show up in either the CGPS $\lambda 21$ cm or the Urumqi $\lambda 6$ cm radio data as expected. The radio source G127.9+1.7, indicated by the red rectangle in Fig. 3, appears in both the CGPS and Urumqi images. Strong infrared emission is seen for some parts of this source in the WISE $12\mu\text{m}$ image. G127.9+1.7 is not recorded in either the WISE H II region catalogue or the Paladini H II region catalogue. However, it is the true Galactic H II region DU 65 collected in Dubout-Crillon (1976). As supporting evidence, we displayed the H α emission of G127.9+1.7 and the flat radio spectrum through TT-plot in the lower panel of Fig. 3 ($T_B \sim \nu^\beta, \beta = \alpha - 2$).

4.1.1. New H II regions

In addition to the missing known extended H II regions in the WISE H II region catalogue, a few new Galactic H II regions and H II region candidates are also discovered in the Urumqi $\lambda 6$ cm survey. They are G68.4+0.2, G76.7–1.2, G94.4+2.7, G139.2–3.0, G139.9–2.0, G172.3+1.9 (H II region candidate), G186.7–4.0 (H II region candidate), G210.8–2.6, and G212.9–3.7. We show them in Fig. 4, Fig. 5, and Fig. 6. For G68.4+0.2, G76.7–1.2, and G94.4+2.7 it is difficult to compare the $\lambda 6$ cm radio emission with the WISE $12\mu\text{m}$ infrared emission due to the large difference in angular resolution. We extracted the $1'$ resolution CGPS $\lambda 21$ cm images and found that the associated infrared emission are not for the entire radio source but for partial shell- or ridge-like structures. The TT-plots confirmed their thermal origin. For the six remaining newly identified H II regions and H II region candidates, we found supporting evidence both in the TT-plot results and the associated H α emission, ex-

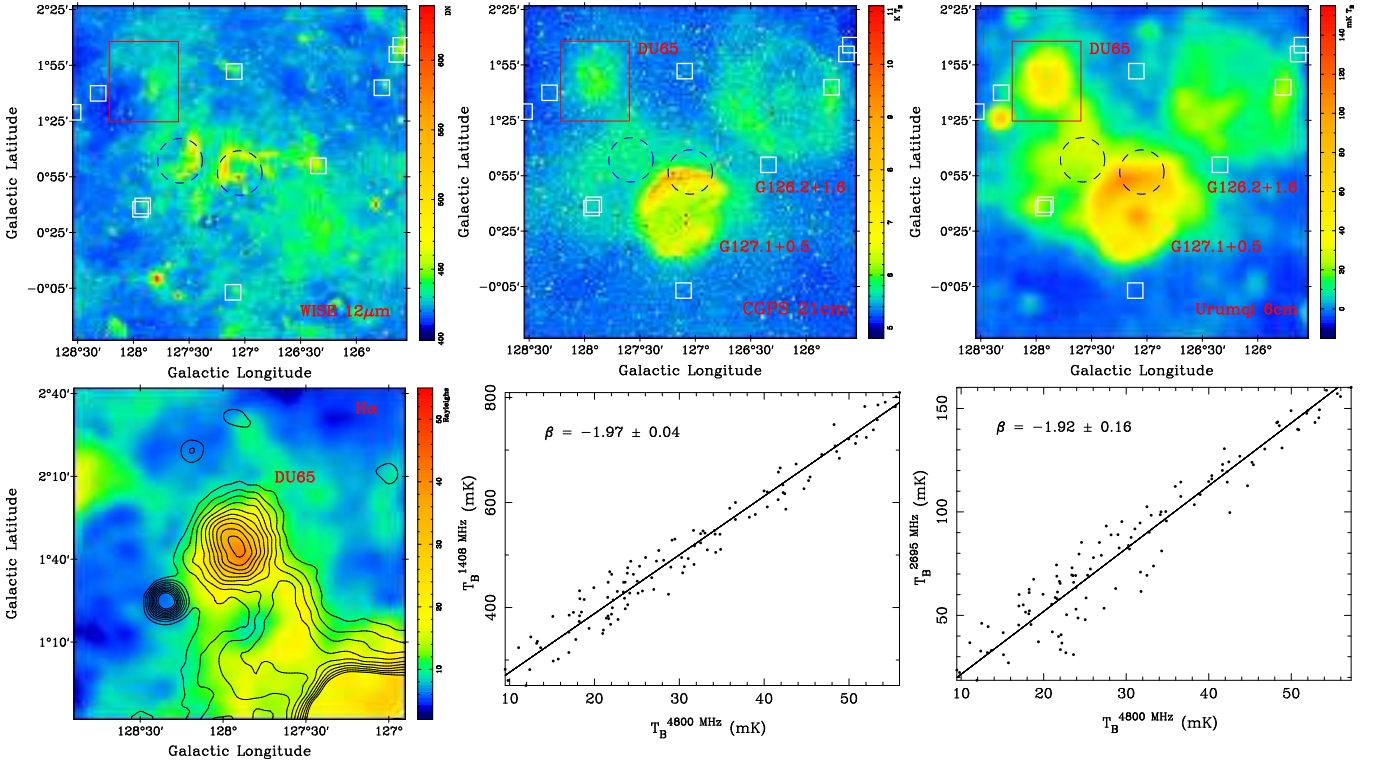


Fig. 3. *Upper panels from left to right:* WISE $12\mu\text{m}$, CGPS $\lambda 21$ cm, and Urumqi $\lambda 6$ cm images centred at $\ell = 127.046$, $b = 0.950$. Small-diameter ($< 7'$) WISE H II regions from Anderson et al. (2014) are marked by white squares, and two extended WISE H II regions (diameter $> 20'$) are indicated by blue dashed circles. Three very extended radio sources in both $\lambda 21$ cm and $\lambda 6$ cm images are SNR G126.2+1.6, SNR G127.1+0.5, and H II region G127.9+1.7 (DU 65, Dubout-Crillon 1976, red rectangle), which is missing in the WISE H II region catalogue. In the *lower left panel*, its H α emission is shown overlaid by the $\lambda 6$ cm total-intensity emission. The *lower middle and lower right panels* show the TT-plot results for DU 65 by using the Urumqi $\lambda 6$ cm against the Effelsberg $\lambda 21$ cm data and the Effelsberg $\lambda 11$ cm data.

cept for G172.3+1.9 and G186.7–4.0. For G172.3+1.9, we did not obtain a reliable TT-plot result and for G186.7–4.0, which is not fully covered by the Effelsberg $\lambda 11$ cm data, the sensitivity of the Effelsberg $\lambda 11$ cm data is not enough for a clear determination. The H α image quality is not high in the south-east part of G172.3+1.9, but the data show a good correlation in the north-east part.

4.1.2. H II regions mistaken as SNRs

Some of the matched WISE H II regions challenge the SNR classification collected in the Green SNR catalogue (Green 2017). G11.183–1.063 is catalogued as a known WISE H II region, but also identified as a shell-type SNR (G11.1–1.0) with a spectral index of $\alpha \sim -0.5$ – -0.6 determined by the VLA $\lambda 90$ cm (11.0 ± 0.3 Jy), the Southern Galactic Plane Survey (SGPS) and VLA $\lambda 21$ cm (4.7 ± 0.8 Jy), and the Effelsberg $\lambda 11$ cm (4.1 ± 0.4 Jy) data (Brogan et al. 2006). By adding the Urumqi $\lambda 6$ cm measurement (3.40 ± 0.25 Jy), Sun et al. (2011a) found a spectral index of $\alpha = -0.41 \pm 0.02$. From Fig. 1 of Sun et al. (2011a), the spectral index fit for G11.1–1.0 strongly depends on the VLA $\lambda 90$ cm result. Based on Effelsberg $\lambda 21$ cm data, Reich et al. (1990b) reported a flux intensity of $S_{21\text{ cm}} = 5.17 \pm 0.52$ Jy closely agreeing with the previous SGPS/VLA result. The $\lambda 11$ cm result of 4.082 Jy from the Effelsberg data is also consistent with the value reported by Brogan et al. (2006). The Urumqi $\lambda 6$ cm result from Reich et al. (2014) is about 4.2 ± 0.2 Jy, a bit higher than that (3.40 ± 0.25 Jy) of Sun et al. (2011a). Using all these values except the $\lambda 90$ cm result, we fit a new spectrum for G11.1–1.0 and found $\alpha = -0.16 \pm 0.07$, im-

plying thermal emission. We show the comparison of the NVSS and WISE $12\mu\text{m}$ data in Fig. 7, the radio and infrared emission of G11.1–1.0 have a very clear and good coincidence. Therefore, G11.1–1.0 seems to favour a H II region origin rather than a SNR identification.

A similar case was found for the source G20.4+0.1 ($\ell = 20.45$, $b = 0.12$) or G20.5+0.2 ($\ell = 20.479$, $b = 0.165$). We found them to be duplicated in the Paladini H II region catalogue (see Sect. 4.2). Brogan et al. (2006) identified G20.47+0.16 to be a shell-type SNR with a spectral index of about $\alpha \sim -0.4$. However, in the WISE H II region catalogue, G20.482+0.169 is a K-type H II region with a similar size of a few arcmins. A flat radio continuum spectrum with $\alpha = -0.08 \pm 0.09$ was found in Sun et al. (2011a) and confirmed in this work (see Fig. 8, *lower panel*). These factors indicate that G20.47+0.16 is not a shell-type SNR, which agrees with the argument in Anderson et al. (2017).

A further investigation is also needed for the source G16.4–0.5. Brogan et al. (2006) identified it as a SNR by revealing a partial shell structure and a steep spectrum with $\alpha = -0.7 \sim -0.8$. Sun et al. (2011a) derived a different spectrum with $\alpha = -0.26 \pm 0.15$. Using a TT-plot between the Effelsberg $\lambda 21$ cm data and the Urumqi $\lambda 6$ cm data, we obtained $\beta = -1.99 \pm 0.04$ (see Fig. 8, *upper panel*). All these results do not support its shell-type SNR nature. The radio emission shown by the NVSS data is fragmented and difficult for a clear match to the WISE infrared emission. More sensitive high angular resolution radio observations are required to determine the shape and the nature of G16.4–0.5.

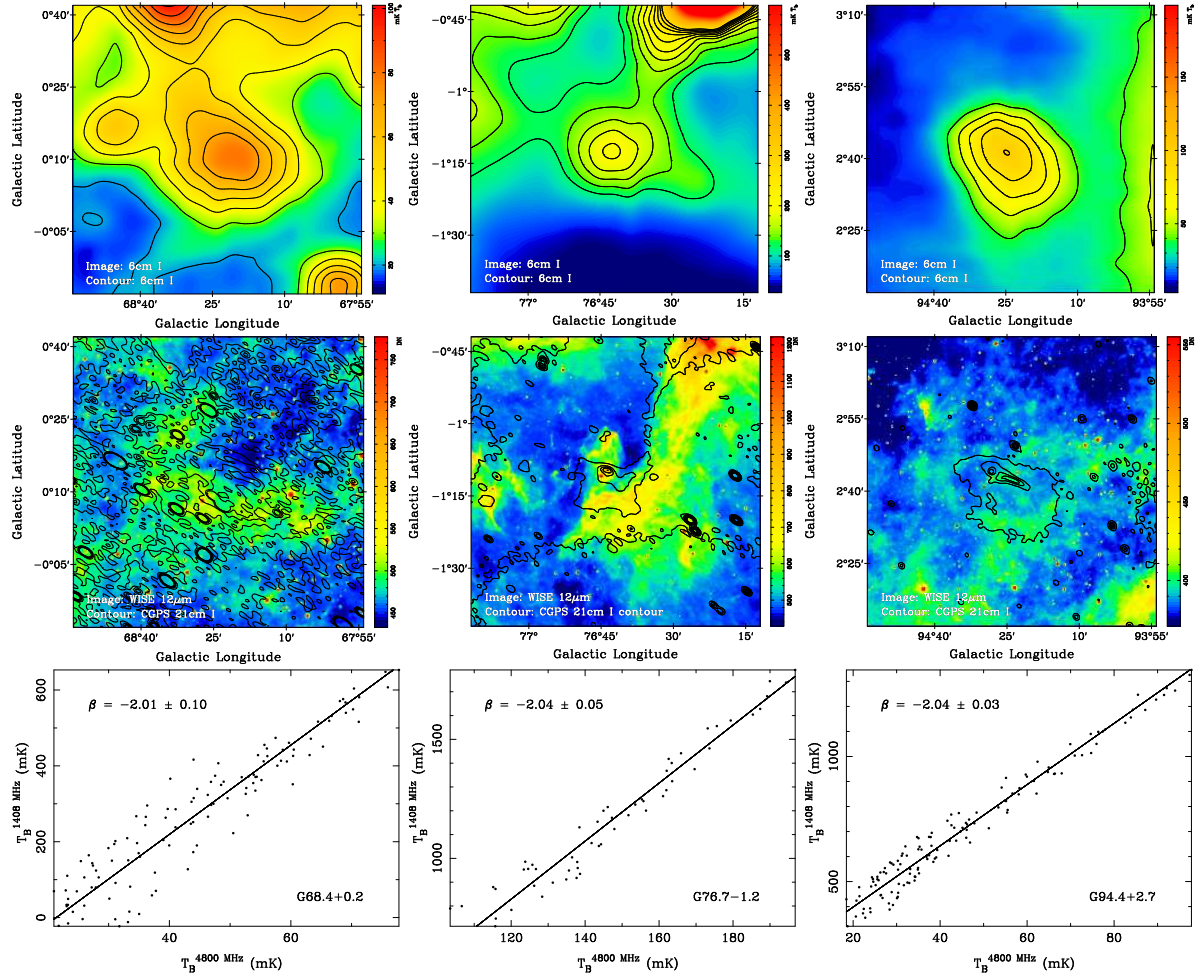


Fig. 4. New H II regions G68.4+0.2, G76.7-1.2, and G94.4+2.7 identified in the Sino-German $\lambda 6$ cm survey. We show $\lambda 6$ cm images and WISE $12\mu\text{m}$ emission overlaid by CGPS 21cm total intensity in the *upper and middle panels*. We present their TT-plot results in the *lower panels*.

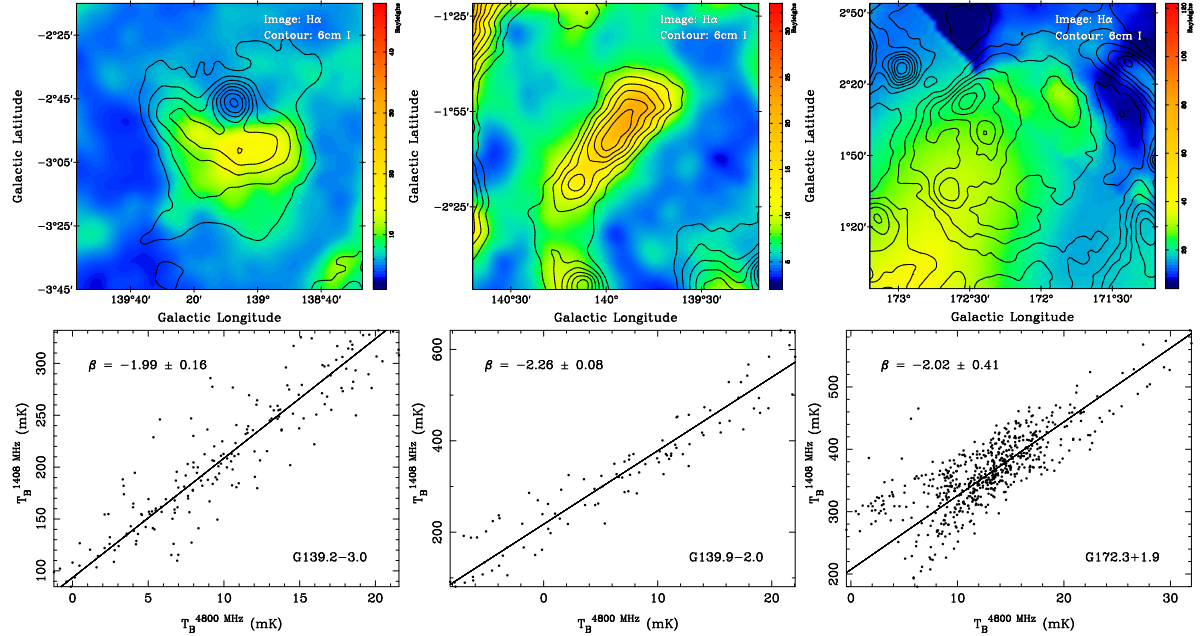


Fig. 5. Newly identified H II regions G139.2-3.0, G139.9-2.0, and G172.3+1.9. H α emission overlaid by Urumqi $\lambda 6$ cm total intensity contours are shown in the *upper panel*. The image quality of the south-east part of G172.3+1.9 is not good; however, correlation can be clearly recognised in the north-west part. TT-plot results are displayed in the *lower panels*.

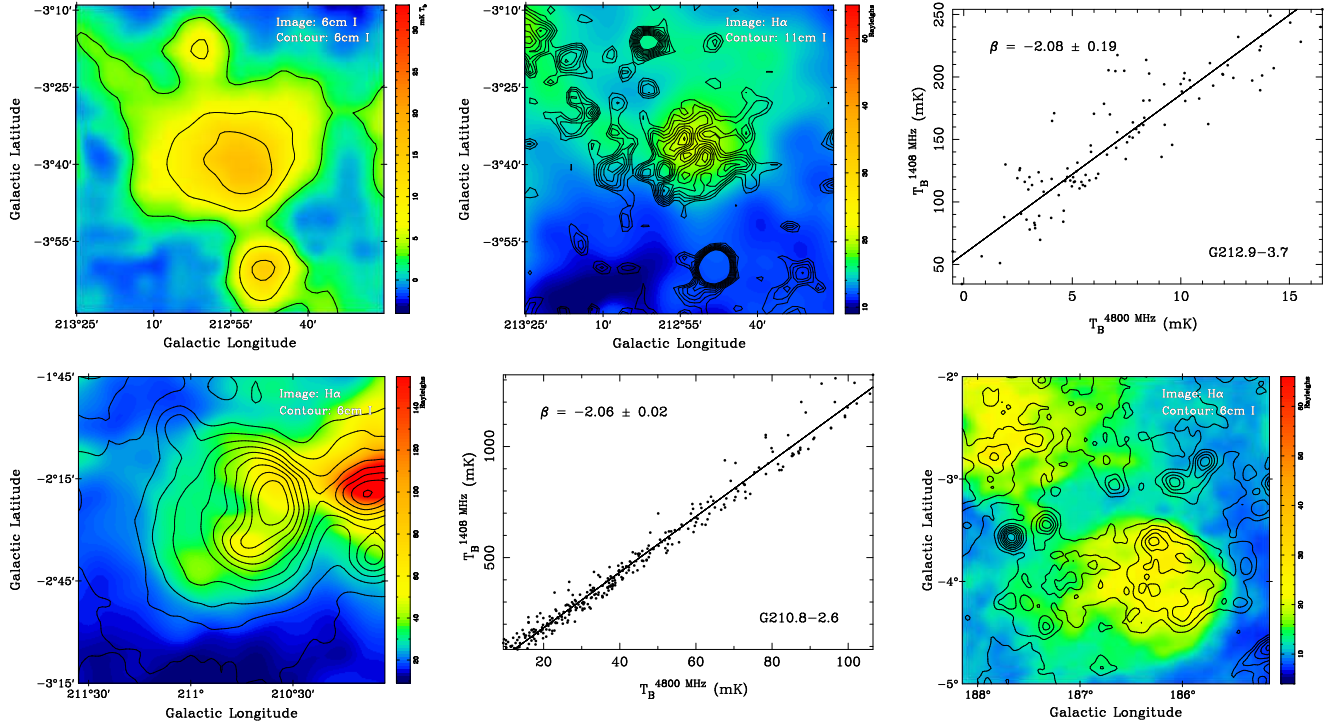


Fig. 6. Upper panel from left to right: $\lambda 6$ cm image, H α emission overlaid by Effelsberg $\lambda 11$ cm total intensity, and the TT-plot result for the new H II region G212.9–3.7. Lower panel from left to middle: H α emission overlaid by Urumqi $\lambda 6$ cm total intensity and the TT-plot result for the new H II region G210.8–2.6. Lower right panel: Same as the lower left panel, but for G186.7–4.0.

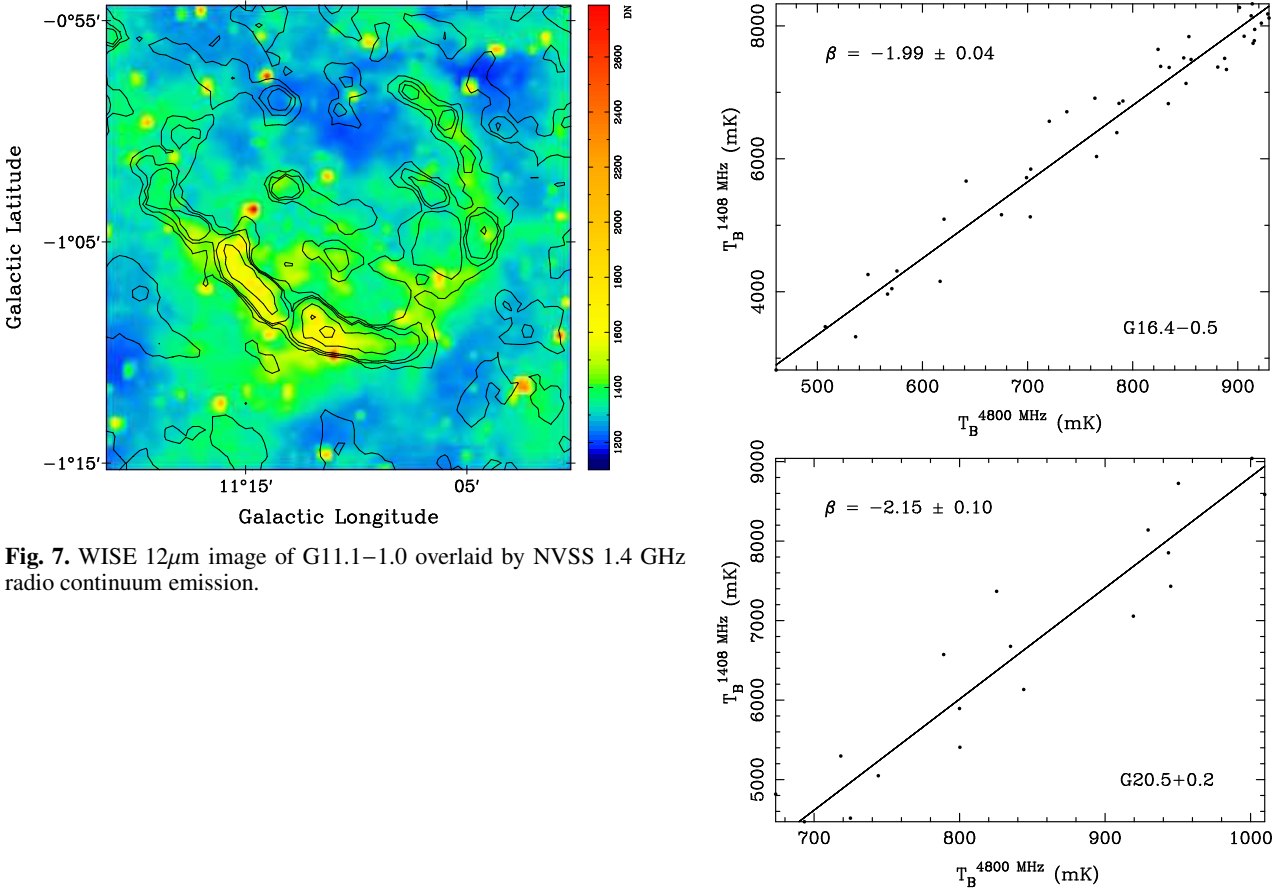


Fig. 7. WISE $12\mu\text{m}$ image of G11.1–1.0 overlaid by NVSS 1.4 GHz radio continuum emission.

Fig. 8. TT-plots for G16.4–0.5 (upper panel) and G20.5+0.2 (lower panel) between Effelsberg $\lambda 21$ cm data and Urumqi $\lambda 6$ cm data.

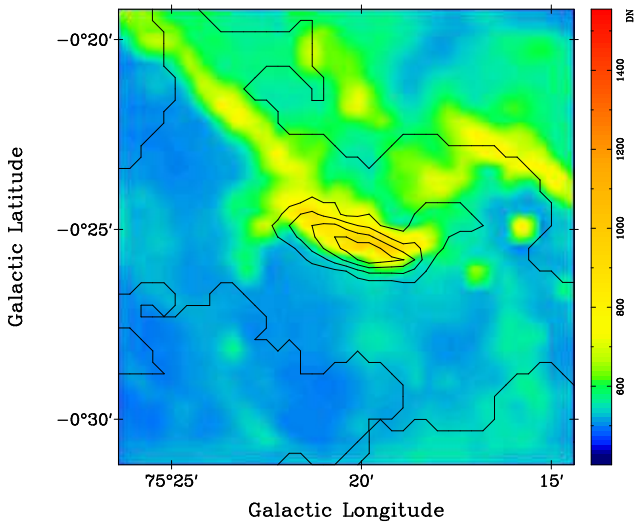


Fig. 9. WISE 12 μ m image of the H II region G75.4–0.4 overlaid by NVSS 1.4 GHz radio continuum emission.

By optical data, G67.8+0.5, a WISE C-type H II region (G67.816+0.511) (Anderson et al. 2014) was identified as a SNR by Sabin et al. (2013). The currently available radio continuum data cannot yield a firm spectrum.

4.2. Notes on some objects in the Paladini H II region catalogue

We cross-matched the small-diameter H II regions in the Paladini catalogue listed in Table 2 with the WISE H II region catalogue. Only a few were found missing in the WISE H II region catalogue, for example G75.4–0.4 (see Fig. 9) and G137.4+0.2. They both show an arc-like structure in the WISE 12 μ m and the NVSS 1.4 GHz images. Their radio spectra are flat, and the infrared and radio emission are morphologically correlated.

Incorrect identifications are found in the Paladini H II region catalogue. Supernova remnants, planetary nebulae, and steep-spectrum objects, likely extragalactic sources were noted. They are listed in Table 5.

Seventeen surveys collected by Paladini et al. (2003) have overlapping regions with the Urumqi λ 6 cm survey (see Table 1). These surveys were conducted from the late 1960s to the 1990s with various radio telescopes at seven different observing frequencies. We were aware of duplications when we noticed that the same remarks (e.g. Westerhout or Sharpless source names) were given to different but very nearby Paladini sources. Therefore, a self-intersection to the sample of the 777 Paladini objects within the λ 6 cm survey area was made. Here we considered a coincidence when $d \leq r_p + r'_p$, where d is the distance of the two centres of the Paladini sources, and r_p and r'_p are the radii of the two adjacent sources. Many duplicated identifications were found and we only discussed the ones which could be confirmed by the Urumqi λ 6 cm data. Different angular resolutions in different surveys accounted for many of the cases. On the one hand, larger beam sizes include more emission and blend the peak position of the fitted centre. On the other hand, as mentioned above, H II regions identified in low angular resolution observations can be resolved into several discrete smaller H II regions in high angular resolution surveys. Different treatments of decimal places of the same source in different literature cause another kind of duplication. We discuss these duplications below. In the follow-

ing, we use the abbreviation ‘PXXX’ (No. XXX source in the Paladini catalogue) for a Paladini object.

1. P134 (010.3, –00.2) and P135 (010.3, –00.1):

Both P134 and P135 are listed as individual point-like sources in the references in Table 2. The difference in designation very likely resulted from the different angular resolutions of the surveys. The similar flux densities achieved for P134 and P135 support that both P134 and P135 indicate the same radio source.

2. P155 (011.9, +00.7) and P156 (011.9, +00.8):

The 4.9 GHz source list of W82 was based on A78. The coordinates of P155 and P156 are so close that none of the given reference surveys can resolve them. It is the radio counterpart of the optical H II region SH 2-38 (Sharpless 1959) as indicated in G70.

3. P164 (012.7, +00.3) and P166 (012.8, +00.4):

P166 (Kuchar & Clark 1997; Altenhoff et al. 1978) is a single isolated radio object. No sources as strong as ~ 2 Jy can be found in its vicinity. K97 obtained a flux density of ~ 2.4 Jy, which is comparable with the results for P164 (SH 2-40, Altenhoff et al. 1970). A78 might have integrated a larger area and obtained a flux density exceeding 7 Jy. The optical image from the red plate of Digitised Sky Survey (Lasker et al. 1990) shows that SH 2-40 consists of several bright knots; this may cause the shift of central coordinates when observed with different angular resolutions.

4. P170 (013.2, +00.0) and P171 (013.2, +00.1):

Based on the 45'' resolution NVSS image, J181405-172832 with a flux density of $S_{1.4 \text{ GHz}} = 2761.8 \pm 85.2$ mJy is the only strong source in this field. The high flux density obtained in various references might result from the low angular resolution which cannot resolve the influence of the ambient emission.

5. P179 (013.9, +00.2) and P180 (013.9, +00.3):

NVSS J181435-164530 ($S_{1.4 \text{ GHz}} = 3307.9 \pm 120.0$ mJy) is the only source that has a comparable flux density to that reported for both P179 and P180 in this area.

6. P189 (014.4, –00.7), P190 (014.4, –00.6) and P192 (014.5, –00.6):

Based on the images from the Effelsberg λ 11 cm data, only one point-like source was identified. Considering that P189, P190, and P192 share similar central coordinates and reported flux densities, they should represent the same source.

7. P199 (015.0, –00.7) / P200 (015.1, –00.9) / P203 (015.2, –00.8) / P204 (015.2, –00.6) and P201 (015.1, –00.7):

From Table 2, it is clear that P199, P200, P203, and P204 are four individual components that are resolved by A78. For the low angular resolution observations of P199 and P201 (e.g. M67, A70), the individual components sum up. It is not

Table 5. 78 misclassifications found in the Paladini H II region catalogue with the Urumqi $\lambda 6$ cm data.

P number	G-NAME	GLong (°)	GLat (°)	Ref	EB S _{21cm} (Jy)	EB S _{11cm} (Jy)	Urumqi S _{6cm} (Jy)	S _{Ref} (Jy)	Freq (GHz)	Ref	Notes
130	G10.1+0.7	10.091	0.727	G70				0.7	2.7	G70	NGC 6537, PN (Condon & Kaplan 1998)
								0.61	10.0	H87	
146	G11.2−0.4	11.172	−0.354	K97				10.367	4.9	K97	SNR G11.2−0.3
								11	2.7	A70	
								11	5.0	A70	
								8.9	5.0	R70	
								5.43	10.0	H87	
147	G11.2+0.1	11.207	0.088	K97		2.72	2.168	2.529	4.9	K97	SNR G11.1+0.1 (Green 2017)
								3.20	4.9	A78	or SNR G11.18+0.11 (Brogan et al. 2006)
157	G11.9+2.2	11.914	2.200	A70	1.74	0.92	0.404	1	1.4	A70	$\alpha = -1.22 \pm 0.09$
								1	2.7	A70	
162	G12.4+3.8	12.434	3.836	A70	4.80	2.40	1.281	4	1.4	A70	$\alpha = -1.08 \pm 0.09$
198	G15.0−1.6	15.041	−1.569	A70				5	1.4	A70	SNR G15.1−1.6
								6	2.7	A70	

Notes. Columns 1 and 2: sequential number in the Paladini catalogue and G-names for sources. Columns 3–5: Galactic coordinates and their references. Columns 6–8: flux densities measured from the Effelsberg $\lambda 21$ cm, $\lambda 11$ cm, and the Urumqi $\lambda 6$ cm data if available. Columns 9–11: flux density at the corresponding frequency, and their reference according to Paladini et al. (2003). The flux densities are reviewed by comparing with those in the original literature. Column 12: remarks why these sources are not considered to be H II regions in this work. Some other references in the 12th column: e.g. Helfand et al. (1989) for P369; Vollmer et al. (2010) for P863. Full table is accessible from the CDS.

clear why D80 gave high values for both P199 (344.5 Jy) and P201 (500 Jy).

8. P218 (016.9, +00.8), P219 (017.0, +00.8), P220 (017.0, +00.9), and P224 (017.1, +00.8):

P218 (G70) and P219 (e.g. A70, R70) is a complex consisting of several components such as P218, P220, and P224 from K97. We measured the extended complex and listed it in Table 4.

9. P221 (017.0, +01.6) and P222 (017.0, +01.7):

G17.0+1.6 (A70) and G17.0+1.7 (G70) were detected by observations with angular resolutions $\geq 8'$. We retrieved the 4/3 resolution Effelsberg $\lambda 11$ cm image and cannot find point-like sources, but we do find an extended and elongated structure. We performed a TT-plot by using the Effelsberg $\lambda 21$ cm data and the Urumqi $\lambda 6$ cm data. The spectral index was found to be $\beta = -2.11 \pm 0.17$ ($\beta = \alpha - 2$), indicating a thermal nature. It is likely that the different designation of P221 and P222 comes from different fitted geometric centres.

10. P232 (018.2, −00.3) and P230 (018.1, −00.3) / P231 (018.2, −00.4) / P233 (018.2, −00.2) / P235 (018.3, −00.4) / P236 (018.3, −0.3) / P239 (018.3, −00.4):

SH 2-53 is a complex consisting of many individual portions as shown in the DSS red plate. The radio emission shown by F87 confirmed the existence of discrete components and extended emission. It is clear that A70, G70, and F87 measured the flux density of the entire structure, while P230, P231, P233, P235 (P239), and P236 from A78 are individual parts of SH 2-53. The low angular resolution flux density measurements may be affected by the nearby SNR G18.1−0.1.

11. P255 (019.2, +02.1) and P256 (019.2, +02.2):

P255 is from the $\sim 11'$ resolution data of A70. P256 comes from the $8'$ resolution data of G70. The 4/3 resolution Effelsberg $\lambda 11$ cm data only show one source. However, this can be further resolved into two discrete sources in the

NVSS data, with flux densities of ~ 2 Jy and ~ 1 Jy, respectively. The spectral index of each source cannot be found in Vollmer et al. (2010). The overall $\alpha_{21-11-6} = -0.52 \pm 0.09$ was obtained by using the Effelsberg $\lambda 21$ cm, $\lambda 11$ cm, and the Urumqi $\lambda 6$ cm data. No WISE counterpart was found for either of the sources. We put P255 and P256 into Table 5, which collects the mis-identifications of the Paladini H II region catalogue.

12. P261 (019.7, −00.1) and P258 (019.6, −00.2) / P259 (019.6, −00.1) / P260 (019.7, −00.2):

Based on the sources identified by A78, P258, P259, and P260 are three individual components that can be resolved by the Effelsberg 4.9 GHz observations. The low angular resolution measurements of G70, A70, and R70 summed the flux densities of discrete portions. K97 listed P258 and P259 as two separated sources with flux densities of 16.6 Jy and 15.2 Jy, respectively. This would double the flux density in this area and contradict the Effelsberg $\lambda 21$ cm and the Urumqi $\lambda 6$ cm measurements, unless they are multi-entries by K97.

13. P266 (020.2, −00.9), P267 (020.3, −00.9) and P268 (020.3, −00.8):

These three entries share similar intrinsic source sizes of about $\sim 10'$ and a consistent flux density of about 3 Jy. We list the source in Table 4 because its apparent size slightly exceeds $16'$, which defines the small-diameter source of the Urumqi $\lambda 6$ cm data.

14. P270 (020.4, +00.1) and P271 (020.5, +00.2):

Both P270 and P271 match the position of the shell-type SNR G20.47+0.16 reported by Brogan et al. (2006). However, this may be a H II region (see detailed discussion in Sect. 4.1).

15. P292 (023.1, +00.5) and P293 (023.1, +00.6):

As pointed out by A70 for P292 and G70 for P293, they are the same H II region SH 2-58.

16. P303 (023.9, +00.1), P304 (023.9, +00.2), and P305 (024.0, +00.2):

The low angular resolution observations of A70 and G70 included the contributions of P303 and P305 by K97 and A78.

17. P317 (024.6, +00.5) and P318 (024.6, +00.6):

Both P317 and P318 indicate the SNR $G_{24.7}+0.6$. We listed them in Table 5.

18. P319/P320 (024.7, -00.2a/b) and P321 (024.7, -00.1):

P319 and P320 are two sources extracted by K97 from radio recombination line observations of Lockman (1989). They are located at $\ell = 24^{\circ}677, b = -0^{\circ}160$ and $\ell = 24^{\circ}742, b = -0^{\circ}207$, and therefore have the same abbreviation as $G_{24.7}-0.2$. Paladini et al. (2003) gave the same flux density information (K97, A78, D80, W82, and W83) for both $G_{24.7}-0.2a$ and $G_{24.7}-0.2b$; however, this seems incorrect. According to the central positions, the peak flux densities and the measured sizes of the sources of K97 and A78, $G_{24.7}-0.2a$ and $G_{24.7}-0.2b$ should have measured flux densities of 9.9 Jy and 3.2 Jy in K97, and 3.19 Jy and 1.42 Jy in A78, respectively. W82 and W83 measured the source centre at $\ell = 24^{\circ}676, b = -0^{\circ}157$ and $\ell = 24^{\circ}68, b = -0^{\circ}16$, which are closer to $G_{24.7}-0.2a$ rather than $G_{24.7}-0.2b$. From the Effelsberg $\lambda 11$ cm image, P321 should be the sum of P319 and P320. However, we cannot explain the high flux densities reported by A70 and G70.

19. P333 (026.1, -00.1) and P334 (026.1, -00.0):

By inspecting the NVSS and the Effelsberg $\lambda 11$ cm images, we identified only one corresponding $\lambda 11$ cm radio source with comparable flux densities.

20. P337 (026.5, +00.4) and P340 (026.6, +00.4):

The same case as P333/P334.

21. P343 (027.3, -00.2) and P344 (027.3, -00.1):

From the image of A78, $G_{27.3}-0.1$ is a single point-like source on a curved ridge. The SNR $G_{27.4}+0.0$ is nearby. The low angular resolution observations could possibly include the contribution of the unrelated emission and therefore overestimated the flux density. The 5 GHz observation of R70 measured a size of 6.3×13.7 for $G_{27.3}-0.2$. The elongation was possibly due to the inclusion of the point-like source itself and the underlying ridge.

22. P362 (028.8, +03.5) and P363 (028.9, +03.5):

Both P362 and P363 are marked as the H II region SH 2-64/W40. The transformation from RA-DEC to L-B coordinates for P363 actually gives $\ell = 28^{\circ}789, b = +3^{\circ}488$, the same as P362.

23. P386 (030.7, -00.0) and P387 (030.8, -00.0):

Both P386 and P387 are the H II region W43.

24. P398 (031.4, -00.3) and P399 (031.4, -00.2):

By inspecting the low angular resolution images, P398 from A70 and P399 from B69 are the same point-like source. For P399, the transformation from RA-DEC to L-B coordinates results in $\ell = 31^{\circ}43, b = -0^{\circ}25$, which should lead to the same G-name as P398.

25. P403 (031.8, +01.5), P404 (031.9, +01.3), and P405 (031.8, +01.4):

$G_{31.8}+1.4$ (P405) was reported to be the H II region SH 2-69 in F72 (see the Erratum of F72). P404 was marked as the H II region RCW 177 in A70. According to Dubout-Crillon (1976), SH 2-69 and RCW 177 share the same coordinates, implying the same identity. In the high angular resolution NVSS image, SH 2-69 shows a bubble-like structure. Regarding the low flux density measured for P403, K97 might only have measured a portion of the source.

26. P406 (032.1, -00.7) and P408 (032.2, +00.1):

B69 gave an incorrect G-name for P406. According to the given RA-DEC coordinates, the centre of the source should be at $\ell = 32^{\circ}133, b = 0^{\circ}117$, very close to P408 at $\ell = 32^{\circ}151, b = 0^{\circ}133$. According to the NVSS image, only one matched point source is found in the field.

27. P419 (034.3, +00.1) and P420 (034.3, +00.2):

We compared the NVSS and the Effelsberg $\lambda 11$ cm images. Considering the similar central positions and the flux densities reported for P419 and P420, they indicate the same radio source.

28. P421 (034.5, -01.1) and P422 (034.6, -01.1):

The coordinates of P421 given by K97 is $\ell = 34^{\circ}550, b = -1^{\circ}110$. The G-name should be written as $G_{34.6}-1.1$, the same as P422. The Effelsberg $\lambda 11$ cm data only shows one source that is slightly extended in the field. No flux density information was found for P422 in B69.

29. P431 (035.2, -01.8) and P432 (035.2, -01.7):

For P431 and P432, the difference in coordinates is very small (see Table 2). Only one corresponding radio source is identified in the Effelsberg $\lambda 11$ cm image.

30. P435 (035.3, -01.8) and P437 (035.4, -01.8):

The same case as P431/P432.

31. P440 (035.6, -00.0), P441 (035.6, +00.1), and P442 (035.7, -00.0):

P441, P442, and the high angular resolution measurements of P440 (e.g. A78, D80) are small discrete components, while the low angular resolution results of P440 from A70 and B69 cannot resolve individual parts but the entire structure.

32. P444 (036.3, -01.7), P445 (036.3, -01.6), P447 (036.4, -01.8), and P448 (036.4, -01.6):

F72 reported that the $17'$ diameter source P448 is the radio counterpart of the H II region SH 2-72 with the optical centre at $\ell = 36^\circ 4', b = -1^\circ 7'$. P445 was marked by B69 as RCW 179 with a diameter of $15'$, while P444 from A70 was also marked as RCW 179, having a size of $15' \times 16'$. SH 2-72 and RCW 179 are the same H II region as indicated in Dubout-Crillon (1976). This is also supported by their similar flux densities and sizes. K97 identified two sources P444 and P447 with flux densities of 3.2 Jy and 0.8 Jy, respectively. They might be small individual components which are included in this extended structure.

33. P449 (036.5, -00.2) and P450 (036.5, -00.1):

The $\lambda 6$ cm source at $\ell = 36^\circ 46', b = -0^\circ 17'$ is the only source that is close to P449 and P450. As supporting evidence, only one ring-like corresponding source is found in the NVSS data.

34. P466 (037.8, -00.3), P468 (037.9, -00.4), P469 (037.9, -00.3):

Based on the NVSS image, P468 (except for the result of R70) is a single point-like component which is included in the low angular resolution measurements of P466 and P469.

35. P477 (039.3, -00.1) and P478 (039.3, -00.0):

Both P477 (W82) and P478 (A70, D70) are marked as NRAO 591.

36. P480 (039.5, $+00.5$) and P484 (039.6, $+00.6$):

P480 and P484 have similar sizes and flux densities, as reported. Only one extended radio structure can be identified in the Effelsberg $\lambda 11$ cm survey data.

37. P487 (039.9, -01.4), P488 (039.9, -01.3), and P494 (040.0, -01.3):

We converted the RA-DEC coordinates reported by F72 to L-B coordinates for P487. The centre is $\ell = 39^\circ 920', b = -1^\circ 355'$, very close to P488 centred at $\ell = 39^\circ 904', b = -1^\circ 351'$. P494 was marked as RCW 182 by A70 and P487 was recognised as SH 2-74 by F72. By comparing the sizes and positions in Rodgers et al. (1960) and Sharpless (1959), RCW 182 and SH 2-74 indicate the same H II region.

38. P490 (039.9, -00.2) and P491 (039.9, -00.1):

P490 was identified by the 8.2 resolution Parkes data (D70), while P491 was from the $\sim 11'$ resolution NRAO data of A70. From a sharper view of the 4.3 resolution Effelsberg $\lambda 11$ cm image, we identified only one matching source at $\ell = 39^\circ 853', b = -0^\circ 180'$.

39. P501 (041.4, $+00.4$) and P505 (041.5, $+00.4$):

Both P501 and P505 indicate the SNR G41.5+0.4. They are listed in Table 5.

40. P503 (041.5, $+00.0$) and P504 (041.5, $+00.1$):

Considering the small differences in positions and flux densities, we identify P503 and P504 to be the same source after inspecting the NVSS and the Effelsberg $\lambda 11$ cm image.

41. P511 (042.4, -0.3), P512 (042.5, -00.2), and P513 (042.6, -00.1):

P512 from low angular resolution observations of A70 and D70 is reported to be an extended source. It contains small individual components that can be resolved in higher angular resolution images. P511 and P513 from K97 are two of the individual components inside P512.

42. P519 (043.3, $+00.5$) and P520 (043.4, $+00.5$):

By converting RA-DEC to L-B coordinates for P519, we found that the G-name of P519 should be written as 043.4+00.5, the same as P520.

43. P524 (043.9, -00.8) and P525 (043.9, -00.7):

We compared the NVSS and the Effelsberg $\lambda 11$ cm images and found the $\lambda 11$ cm source located at $\ell = 43^\circ 896', b = -0^\circ 801'$ is the only matching one.

44. P529 (044.2, $+00.1$) and P531 (044.3, $+00.1$):

The same case as P524/P525.

45. P530 (044.3, -00.4) and P532 (044.4, -00.3):

The same case as P524/P525.

46. P540 (045.4, $+00.1$) and P541 (045.5, $+00.1$):

Both P540 from D70 and P541 from A70 were marked as the radio source NRAO 601. Paladini et al. (2003) only listed one corresponding source for P541; we found the second component in A78/D80, W82, and W83. The sum of the two components agreed well with the results obtained from the low angular resolution observations (see Table 2).

47. P564 (049.5, -00.4) / P559 (049.3, -00.3), P561 (049.4, -00.5), P562 (049.4, -00.3), P563 (049.4, -00.2), P567 (049.6, -00.4):

The low angular resolution observations of W51A, such as A70 for P564, smear out the individual structures (P559, P561, P562, P563, P567) that can be resolved by high angular resolution observations. It is not clear why the K97 measurements toward P561 and P564 both exceed 100 Jy, which result in a much larger flux density for W51A.

48. P570 (050.0, -00.1) and P571 (050.0, -00.0):

The same case as P524/P525.

49. P578 (051.2, -00.1) and P579 (051.2, $+00.1$):

P578 has a measured size of 20.9×22.4 and a flux density of 37 Jy in R70, while A70 measured a similar size of $20' \times 20'$ and comparable flux density of 35 Jy for P579. Considering the similar size and flux density, P578 and P579 should be the same source. It is embedded in a complex

spanning over 1° (see Table 4). P576 and P580 are also included in this complex.

50. P597 (054.1, -00.1) and P598 (054.1, -00.0):

A70 suspected that the source P598 might be the steep-spectrum radio source 4C+18.57. From the NVSS image, 4C+18.57 is a single point-like source close to P597. These two objects cannot be resolved by the observation of A70. Thus, the measured flux density of P598 included the contribution of the H II region P597 and of 4C+18.57. It is not easy to obtain an accurate flux density for P597 with the Urumqi data due to the influence of the nearby SNR G54.4-0.3.

51. P605 (057.5, -00.3) and P606 (057.6, -00.3):

The same case as P524/P525.

52. P619 (063.1, $+00.4$), P620 (063.2, $+00.4$), and P621 (063.2, $+00.5$):

The same case as P524/P525. They are the H II region SH 2-90.

53. P624 (064.1, -00.5) and P626 (064.2, -00.5):

Both P624 (F72) and P626 (A70) are marked as the H II region SH 2-93.

54. P632 (068.1, $+00.9$), P633 (068.1, $+01.0$), and P634 (068.2, $+01.0$):

P633 from F72 and P634 from A70 are both reported as an extended source and marked as the H II region SH 2-98. They are incorporated in the $\lambda 6$ cm extended H II region G68.20+1.05 in Table 4. From the high-resolution CGPS image, SH 2-98 is a ring-like structure with a diameter of about $25'$. P632 from K97 is a bright, small-diameter ($\sim 2'$) source situated on the southern part of the ring. It can hardly be resolved in the low angular resolution observations such as A70 and F72. Therefore, the flux density measurements by A70 and F72 contain the entire ring structure and P632, while K97 only measure the point-like source. Due to influence of the ring structure, Reich et al. (2014) obtain a higher flux density for P632 than obtained by K97.

55. P636 (069.9, $+01.5$) and P637 (069.9, $+01.6$):

In the $\lambda 6$ cm image, P636 is a point-like source which is somehow confused by the radio emission in its north. Low angular resolution observations might overestimate the flux density. A good fit for the thermal radio spectrum was obtained through the Effelsberg $\lambda 21$ cm, $\lambda 11$ cm, and the Urumqi $\lambda 6$ cm data. However, it is strange that with the angular resolution similar to the Effelsberg $\lambda 21$ cm data and the Urumqi $\lambda 6$ cm data, $S_{2.7\text{GHz}} = 14$ Jy from A70 is so high.

56. P651 (074.8, $+00.6$) and P652 (074.8, $+00.7$):

P651 from F72 and P652 from A70 were both proposed as the counterpart of the H II region SH 2-104. All the flux density estimates are consistent, except that by F72. With the angular resolution similar to the Urumqi data, the large

flux density of 32.2 Jy is unclear.

57. P668 (078.0, $+00.6$) and P669 (078.1, $+00.6$):

P668 is reported to be a point-like source with an intrinsic size of about $3'$ in K97 and R70. This can be confirmed by the Effelsberg $\lambda 11$ cm data. The source is isolated. W70 reported that P669 has a flux density of 18.5 Jy and a size of $9' \times 7'$ after deconvolution. These results are difficult to explain.

58. P696 (078.9, $+03.7$) and P699 (079.0, $+03.6$):

P699 was measured by W70 to have an intrinsic size of $28' \times 20'$, while P696 has a larger source size of $37.2' \times 37.9'$ in R70. Considering the large size and the small difference between the central coordinates, P696 and P699 obviously indicate the same object.

59. P721 (080.0, $+00.8$) and P722 (080.0, $+00.9$):

P722 from K97 can be confirmed as a single point-like source by the Effelsberg $\lambda 11$ cm data, which has a similar angular resolution. W70 obtained an intrinsic source size of $16' \times 16'$ for P721, which encompasses the source of P722. The measured flux density of 17 Jy might result from the integration of a larger area.

60. P723 (080.0, $+01.5$) and P726 (080.1, $+01.5$):

This duplication arises from different sizes found in different literature. For the same source P723, K97 reported an intrinsic source size of about $6'$, but R70 reported $21.1' \times 35.5'$. For P726, W70 found $12' \times 22'$. The 4.3 angular resolution Effelsberg $\lambda 11$ cm image shows an elongated structure rather than a point-like source. The different values for P723/P726 might result from the different areas selected for the flux density integration.

61. P733 (080.4, $+00.4$) and P734 (080.4, $+00.5$):

W70 measured an intrinsic size of $17' \times 22'$ for P733, while R70 measured $4.4' \times 32.2'$ for P734. The two extended objects overlap and should be the same source. K97 obtained a much smaller size of about $5'$ for P733. According to the Effelsberg $\lambda 11$ cm image, which has a similar angular resolution to that of K97, K97 very probably measured only the compact central part of the source.

62. P738 (80.8, $+00.4$) and P743 (080.9, $+00.4$):

P743 was identified by K97 and R70 with a size of about $4'$. It appears as a point-like source in the Effelsberg $\lambda 11$ cm and Urumqi $\lambda 6$ cm images. The flux density measurements by K97 and R70 can be clearly supported by the Effelsberg $\lambda 11$ cm and the Urumqi $\lambda 6$ cm data. P738 was identified by W70 with a much higher flux density of $S_{2.7\text{GHz}} = 43.2$ Jy and a much larger size of $17' \times 16'$. We cannot explain the W70 result with the current data.

63. P741 (80.9, -00.2) and P742 (080.9, -00.1):

High angular resolution observations of P741 and P742 region from the CGPS data shows a circular emission region

($\sim 12'$) with a bright source on its north-east edge. A thin shell structure ($\sim 10'$), which does not seem to be related, runs underneath the circular region. By overlaying the 87GB/GB6 sources on the image, it is possible that K97 only measured the upper bright part of the structure. At an angular resolution of about $10'$ (e.g. R70 and W70), these structures can no longer be resolved but seen as a single point-like source.

64. P789 (097.5, +03.2) and P790 (097.6, +03.2):

The same case as P524/P525.

65. P798 (104.6, +01.3) and P799 (104.6, +01.4):

The H II region SH 2-135 has an oval shape with a size of $22' \times 15'$ (Lynds 1965). K97 only measured the bright knots (P799) in its northern part, while F72 measured the entire structure (P798).

66. P812 (108.8, -01.0) and P813 (108.8, -00.9):

Based on Sharpless (1959), SH 2-152 ($\ell = 108^\circ 8, b = -0^\circ 9$) and SH 2-153 ($\ell = 108^\circ 8, b = -1^\circ 0$) are two very close H II regions which the Urumqi $\lambda 6$ cm observation cannot resolve. The flux density measurement by K97 may include both SH 2-152 and SH 2-153. The coordinate of P813 from W83 is $\ell = 108^\circ 76, b = -0^\circ 950$. The abbreviation should be the same as P812. W83 has a much better angular resolution than K97, who only measured SH 2-152.

67. P817 (110.1, +00.0) and P818 (110.1, +00.1):

Both P817 from F72 and K97 and P818 from W83 are the H II region SH 2-156.

68. P830 (115.0, +03.1) and P831 (115.0, +03.2):

The same as the case of P524/P525.

69. P839 (119.4, -00.9) and P840 (119.4, -00.8):

Based on the image of Effelsberg $\lambda 11$ cm data, P839 from F72 is the H II region SH 2-173 with a circular shape and a bright western shell. From the coordinates given by K97 for P840, it is likely that K97 measured the western shell of SH 2-173 only.

70. P854 (136.4, +02.5) and P856 (136.5, +02.5):

The same as the case of P524/P525.

71. P866 (151.6, -00.3) and P867 (151.6, -00.2):

Both P866 from F72 and P867 from W83 were claimed to be the H II region SH 2-209, which consists of a northern component SH 2-209 N ($\ell = 151^\circ 59, b = -0^\circ 22$) and a southern component SH 2-209 S ($\ell = 151^\circ 64, b = -0^\circ 47$). F72 reported a lower central position, which might be influenced by SH 2-209 S.

72. P869 (154.6, +02.4) and P870 (154.7, +02.4):

The same as the case of P524/P525.

73. P887 (180.8, +04.0) and P888 (180.9, +04.1):

P888 from F72 is thought to be the radio counterpart of the H II region SH 2-241. In the NVSS image, P888 mainly includes the source J060358+301522 ($\ell = 180^\circ 87, b = +4^\circ 11$) and an area of diffuse emission in its south-east. It resembles the optical image of the H II region in the DSS red plate. P887 ($\ell = 180^\circ 79, b = +4^\circ 03$) is catalogued by K97, but cannot be found in either the 87GB or the GB6 catalogue. We convolved the NVSS image to an angular resolution of $3.7'$, the same as K97. However, we failed to identify any source at $\ell = 180^\circ 79, b = +4^\circ 03$. The source J060358+301522 has a flux density of about $S_{1.4 \text{ GHz}} = 140$ mJy and a spectral index of $\alpha = -0.06$ (Vollmer et al. 2010). It was also identified in the GB6 catalogue with a consistent flux density of $S_{4.85 \text{ GHz}} = 158$ mJy. Considering the similar flux density reported by K97 ($S_{K97} = 0.164$ Jy), it might be that P887 indicates the source NVSS J060358+301522, but is listed with wrong coordinates.

74. P896 (192.1, +03.6) and P897 (192.2, +03.6):

F72 reported that P896 is the H II region SH 2-253, whose optical centre is at $\ell = 192^\circ 2, b = +3^\circ 6$. It appears as an elongated diffuse structure both in the Effelsberg $\lambda 11$ cm and in the Urumqi $\lambda 6$ cm images. A similar optical morphology was seen in the DSS red plate. K97 gave a very small size and flux density for P897, which likely accounts for a part of the entire H II region.

75. P905 (196.4, -01.7) and P906 (196.5, -01.7):

The same as the case of P524/P525.

76. P909 (197.8, -02.4) and P910 (197.8, -02.3):

From the NVSS image, a strong radio source is located at $\ell = 197^\circ 78, b = -2^\circ 32$ (P910) and a few weak sources are visible around $\ell \sim 197^\circ 76, b \sim -2^\circ 45$. They show up as two radio sources in the 4.3 resolution Effelsberg $\lambda 11$ cm image. They cannot be separated in the 9.5 resolution Urumqi $\lambda 6$ cm data. The same case is expected for P909 from F72.

5. Summary

We identified and analysed H II regions from the Sino-German $\lambda 6$ cm polarisation survey of the $\sim 2200 \text{ deg}^2$ plane area. The small H II regions (apparent size $< 16'$) were obtained by cross-matches between the $\lambda 6$ cm small-diameter sources of Reich et al. (2014), the Paladini radio H II region catalogue, and the WISE infrared H II region catalogue, while the extended H II regions were found by overlaying the Paladini and WISE H II regions onto the Urumqi $\lambda 6$ cm survey image and searching for coincidences by eye. The spectra of the chosen sources were examined by using the Effelsberg $\lambda 21$ cm, $\lambda 11$ cm, together with the Urumqi $\lambda 6$ cm data. Finally, 401 H II regions were extracted from the $\lambda 6$ cm survey. We listed their positions, $\lambda 6$ cm flux densities, and distances if available in Table 2, Table 3, and Table 4.

Multi-frequency and multi-domain observations are important for H II region identification. The WISE H II region catalogue, being currently the largest, provides an excellent sample of small-diameter H II regions, but misses some extended H II regions as listed in Table 4. Among these ~ 30 extended H II regions

that were not present in the WISE H II region catalogue, 9 are revealed in this paper for the first time. In the Urumqi survey area, there are 78 mis-classifications and 76 pairs of duplicated identifications found in the Paladini H II region catalogue. The Mis-classifications were mainly inherited from the literature from the 1970s. They are chosen by spectra check and/or by comparison with the SNR or PN catalogues. The duplications are mostly the results of the inclusion of both high and low angular resolution observations toward the same source.

G11.1–1.0, G20.4+0.1, and G16.4–0.5, were initially identified as SNRs by their shell-like appearance and steep radio continuum spectra (Brogan et al. 2006). However, the newly derived radio spectra of these three sources are all flat, which imply that their nature is thermal. Additionally, G11.1–1.0 (WISE H II region G11.183–1.063), G20.4+0.1 (WISE H II region G20.482+0.169), and G16.4–0.5 (WISE H II region G16.364–0.558) have all been identified as K-type, namely known H II regions in the WISE H II region catalogue, and G11.1–1.0 shows well-correlated radio and infrared emission.

Acknowledgements. We would like to thank Dr. Thomas L. Wilson for the critical reading of the manuscript and the anonymous referee for the helpful comments. The Chinese authors are supported by the National Key R&D Program of China (NO. 2017YFA0402701), the Open Project Program of the Key Laboratory of FAST, NAOC, the Chinese Academy of Sciences, the National Natural Science foundation of China (11303035, 11503033), and the Partner group of the MPIfR at NAOC in the framework of the exchange programme between MPG and CAS for many bilateral visits. XYG acknowledges financial support from the CAS-NWO cooperation programme and Young Researcher Grant of National Astronomical Observatories, Chinese Academy of Sciences, and the FAST FELLOWSHIP. The FAST FELLOWSHIP is supported by Special Funding for Advanced Users, budgeted and administrated by the Center for Astronomical Mega-Science, Chinese Academy of Sciences (CAMS). LGH is grateful for the support by the Youth Innovation Promotion Association CAS. The Digitized Sky Surveys were produced at the Space Telescope Science Institute under U.S. Government grant NAG W-2166. The images of these surveys are based on photographic data obtained using the Oschin Schmidt Telescope on Palomar Mountain and the UK Schmidt Telescope. The plates were processed into the present compressed digital form with the permission of these institutions. The National Geographic Society - Palomar Observatory Sky Atlas (POSS-I) was made by the California Institute of Technology with grants from the National Geographic Society. The Wisconsin H α Mapper and its H α Sky Survey have been funded primarily by the National Science Foundation. The facility was designed and built with the help of the University of Wisconsin Graduate School, Physical Sciences Lab, and Space Astronomy Lab. NOAO staff at Kitt Peak and Cerro Tololo provided on-site support for its remote operation. This publication makes use of data products from the Wide-field Infrared Survey Explorer, which is a joint project of the University of California, Los Angeles, and the Jet Propulsion Laboratory/California Institute of Technology, funded by the National Aeronautics and Space Administration.

References

- Altenhoff, W. J., Downes, D., Goad, L., Maxwell, A., & Rinehart, R. 1970, A&AS, 1, 319
- Altenhoff, W. J., Downes, D., Pauls, T., & Schraml, J. 1978, A&AS, 35, 23
- Anderson, L. D., Armentrout, W. P., Johnstone, B. M., et al. 2015, ApJS, 221, 26
- Anderson, L. D., Armentrout, W. P., Luisi, M., et al. 2018, ApJS, 234, 33
- Anderson, L. D., Bania, T. M., Balser, D. S., et al. 2014, ApJS, 212, 1
- Anderson, L. D., Bania, T. M., Balser, D. S., & Rood, R. T. 2011, ApJS, 194, 32
- Anderson, L. D., Wang, Y., Bihr, S., et al. 2017, A&A, 605, A58
- Bania, T. M., Anderson, L. D., & Balser, D. S. 2012, ApJ, 759, 96
- Beard, M. & Kerr, F. J. 1969, Australian Journal of Physics, 22, 121
- Brogan, C. L., Gelfand, J. D., Gaensler, B. M., Kassim, N. E., & Lazio, T. J. W. 2006, ApJ, 639, L25
- Brunthaler, A., Reid, M. J., Menten, K. M., et al. 2009, ApJ, 693, 424
- Caswell, J. L. & Haynes, R. F. 1987, A&A, 171, 261
- Choi, Y. K., Hachisuka, K., Reid, M. J., et al. 2014, ApJ, 790, 99
- Comerón, F., Pasquali, A., & Torra, J. 2006, A&A, 457, 553
- Condon, J. J., Broderick, J. J., & Seielstad, G. A. 1989, AJ, 97, 1064
- Condon, J. J., Cotton, W. D., Greisen, E. W., et al. 1998, AJ, 115, 1693
- Condon, J. J., Griffith, M. R., & Wright, A. E. 1993, AJ, 106, 1095
- Condon, J. J. & Kaplan, D. L. 1998, ApJS, 117, 361
- Day, G. A., Warne, W. G., & Cooke, D. J. 1970, Aust. J. Phys. Astrophys. Suppl., 13, 11
- Downes, D., Wilson, T. L., Bieging, J., & Wink, J. 1980, A&AS, 40, 379
- Dubout-Crillon, R. 1976, A&AS, 25, 25
- Felli, M. & Churchwell, E. 1972, A&AS, 5, 369
- Fich, M. & Blitz, L. 1984, ApJ, 279, 125
- Finkbeiner, D. P. 2003, ApJS, 146, 407
- Foster, T. & Brunt, C. M. 2015, AJ, 150, 147
- Fragkou, V., Parker, Q. A., Bojčić, I. S., & Aksaker, N. 2018, MNRAS, 480, 2916
- Frew, D. J., Bojčić, I. S., & Parker, Q. A. 2013, MNRAS, 431, 2
- Fürst, E., Reich, W., Reich, P., Handa, T., & Sofue, Y. 1987, A&AS, 69, 403
- Fürst, E., Reich, W., Reich, P., & Reif, K. 1990a, A&AS, 85, 805
- Fürst, E., Reich, W., Reich, P., & Reif, K. 1990b, A&AS, 85, 691
- Gao, X. Y. & Han, J. L. 2013, A&A, 551, A16
- Gao, X. Y., Han, J. L., Reich, W., et al. 2011, A&A, 529, A159
- Gao, X. Y., Reich, W., Han, J. L., et al. 2010, A&A, 515, A64
- Goss, W. M. & Day, G. A. 1970, Aust. J. Phys. Astrophys. Suppl., 13, 3
- Goss, W. M. & Shaver, P. A. 1970, Aust. J. Phys. Astrophys. Suppl., 14, 1
- Graham, D. A., Haslam, C. G. T., Salter, C. J., & Wilson, W. E. 1982, A&A, 109, 145
- Green, D. A. 2017, VizieR Online Data Catalog, 7278
- Handa, T., Sofue, Y., Nakai, N., Hirabayashi, H., & Inoue, M. 1987, PASJ, 39, 709
- Harvey-Smith, L., Madsen, G. J., & Gaensler, B. M. 2011, ApJ, 736, 83
- Haynes, R. F., Caswell, J. L., & Simons, L. W. J. 1978, Aust. J. Phys. Astrophys. Suppl., 45, 1
- Haynes, R. F., Caswell, J. L., & Simons, L. W. J. 1979, Aust. J. Phys. Astrophys. Suppl., 48, 1
- Helfand, D. J., Velusamy, T., Becker, R. H., & Lockman, F. J. 1989, ApJ, 341, 151
- Honma, M., Bushimata, T., Choi, Y. K., et al. 2007, PASJ, 59, 889
- Hou, L. G. & Han, J. L. 2014, A&A, 569, A125
- Hou, L. G., Han, J. L., & Shi, W. B. 2009, A&A, 499, 473
- Immer, K., Reid, M. J., Menten, K. M., Brunthaler, A., & Dame, T. M. 2013, A&A, 553, A117
- Irabor, T., Hoare, M. G., Oudmaijer, R. D., et al. 2018, MNRAS, 480, 2423
- Kim, I.-J., Pyo, J., Jeong, W.-S., et al. 2018, ApJS, 238, 28
- Kuchar, T. A. & Clark, F. O. 1997, ApJ, 488, 224
- Landecker, T. L., Reich, W., Reid, R. I., et al. 2010, A&A, 520, A80
- Lasker, B. M., Sturch, C. R., McLean, B. J., et al. 1990, AJ, 99, 2019
- Lockman, F. J. 1989, ApJS, 71, 469
- Lynds, B. T. 1965, ApJS, 12, 163
- Makai, Z., Anderson, L. D., Mascoop, J. L., & Johnstone, B. 2017, ApJ, 846, 64
- Mezger, P. G. & Henderson, A. P. 1967, ApJ, 147, 471
- Miszalski, B., Parker, Q. A., Acker, A., et al. 2008, MNRAS, 384, 525
- Miville-Deschênes, M. & Lagache, G. 2005, ApJS, 157, 302
- Moisés, A. P., Damineli, A., Figuerêdo, E., et al. 2011, MNRAS, 411, 705
- Moscadelli, L., Reid, M. J., Menten, K. M., et al. 2009, ApJ, 693, 406
- Oh, C. S., Kobayashi, H., Honma, M., et al. 2010, PASJ, 62, 101
- Paladini, R., Burigana, C., Davies, R. D., et al. 2003, A&A, 397, 213
- Parker, Q. A., Acker, A., Frew, D. J., et al. 2006, MNRAS, 373, 79
- Parker, Q. A., Bojčić, I. S., & Frew, D. J. 2016, in Journal of Physics Conference Series, Vol. 728, Journal of Physics Conference Series, 032008
- Reich, P. & Reich, W. 1986, A&AS, 63, 205
- Reich, P., Reich, W., & Fürst, E. 1997, A&AS, 126, 413
- Reich, W. 1982, A&AS, 48, 219
- Reich, W., Fürst, E., Haslam, C. G. T., Steffen, P., & Reif, K. 1984, A&AS, 58, 197
- Reich, W., Fürst, E., Reich, P., & Reif, K. 1990a, A&AS, 85, 633
- Reich, W., Fürst, E., Reich, P., Sofue, Y., & Handa, T. 1986, A&A, 155, 185
- Reich, W., Reich, P., & Fürst, E. 1990b, A&AS, 83, 539
- Reich, W., Sun, X. H., Reich, P., et al. 2014, A&A, 561, A55
- Reid, M. J., Menten, K. M., Brunthaler, A., et al. 2009, ApJ, 693, 397
- Reifenstein, E. C., Wilson, T. L., Burke, B. F., Mezger, P. G., & Altenhoff, W. J. 1970, A&A, 4, 357
- Rodgers, A. W., Campbell, C. T., & Whiteoak, J. B. 1960, MNRAS, 121, 103
- Russell, D. 2003, A&A, 397, 133
- Russeil, D., Adami, C., & Georgelin, Y. M. 2007, A&A, 470, 161
- Rygl, K. L. J., Brunthaler, A., Reid, M. J., et al. 2010, A&A, 511, A2
- Rygl, K. L. J., Brunthaler, A., Sanna, A., et al. 2012, A&A, 539, A79
- Sabin, L., Parker, Q. A., Contreras, M. E., et al. 2013, MNRAS, 431, 279
- Sanna, A., Reid, M. J., Menten, K. M., et al. 2014, ApJ, 781, 108
- Sharpless, S. 1959, ApJS, 4, 257
- Shi, W., Sun, X., Han, J., Gao, X., & Xiao, L. 2008, Chinese Journal of Astronomy and Astrophysics, 8, 575
- Sieber, W. & Seiradakis, J. H. 1984, A&A, 130, 257
- Sofue, Y. & Reich, W. 1979, A&AS, 38, 251
- Su, H., Hurley-Walker, N., Jackson, C. A., et al. 2017, MNRAS, 465, 3163

- Suad, L. A., Cichowolski, S., Arnal, E. M., & Testori, J. C. 2012, A&A, 538, A60
- Sun, X. H., Han, J. L., Reich, W., et al. 2007, A&A, 463, 993
- Sun, X. H., Reich, P., Reich, W., et al. 2011a, A&A, 536, A83
- Sun, X. H., Reich, W., Han, J. L., Reich, P., & Wielebinski, R. 2006, A&A, 447, 937
- Sun, X. H., Reich, W., Han, J. L., et al. 2011b, A&A, 527, A74
- Tasker, N. J., Condon, J. J., Wright, A. E., & Griffith, M. R. 1994, AJ, 107, 2115
- Taylor, A. R., Gibson, S. J., Peracaula, M., et al. 2003, AJ, 125, 3145
- Turtle, A. J., Pugh, J. F., Kenderdine, S., & Pauliny-Toth, I. I. K. 1962, MNRAS, 124, 297
- Vollmer, B., Gassmann, B., Derrière, S., et al. 2010, A&A, 511, A53
- Wendker, H. J. 1970, A&A, 4, 378
- Wilson, T. L., Mezger, P. G., Gardner, F. F., & Milne, D. K. 1970, A&A, 6, 364
- Wink, J. E., Altenhoff, W. J., & Mezger, P. G. 1982, A&A, 108, 227
- Wink, J. E., Wilson, T. L., & Bieging, J. H. 1983, A&A, 127, 211
- Wu, Y. W., Sato, M., Reid, M. J., et al. 2014, A&A, 566, A17
- Xiao, L., Han, J. L., Reich, W., et al. 2011, A&A, 529, A15
- Xu, W. F., Gao, X. Y., Han, J. L., & Liu, F. S. 2013a, A&A, 559, A81
- Xu, Y., Li, J. J., Reid, M. J., et al. 2013b, ApJ, 769, 15
- Xu, Y., Reid, M. J., Zheng, X. W., & Menten, K. M. 2006, Science, 311, 54
- Zhang, B., Moscadelli, L., Sato, M., et al. 2014, ApJ, 781, 89
- Zhang, B., Reid, M. J., Menten, K. M., et al. 2013, ApJ, 775, 79
- Zhang, B., Zheng, X. W., Reid, M. J., et al. 2009, ApJ, 693, 419